Stardust Interstellar Preliminary Examination II: Curating the interstellar dust collector, picokeystones, and sources of impact tracks

David R. FRANK[1*], Andrew J. WESTPHAL[2], Michael E. ZOLENSKY[3], Zack GAINSFORTH[2],
Anna L. BUTTERWORTH[2], Ronald K. BASTIEN[1], Carlton ALLEN[3], David ANDERSON[2],
Asna ANSARI[4], Sasa BAJT[5], Nabil BASSIM[6], Hans A. BECHTEL[7], Janet BORG[8],
Frank E. BRENKER[9], John BRIDGES[10], Donald E. BROWNLEE[11], Mark BURCHELL[12],
Manfred BURGHAMMER[13], Hitesh CHANGELA[14], Peter CLOETENS[13], Andrew M. DAVIS[15,4],
Ryan DOLL[16], Christine FLOSS[16], George FLYNN[17], Eberhard GRÜN[18], Philipp R. HECK[4],
Jon K. HILLIER[19], Peter HOPPE[20], Bruce HUDSON[21], Joachim HUTH[20], Brit HVIDE[4],
Anton KEARSLEY[22], Ashley J. KING[15], Barry LAI[23], Jan LEITNER[20], Laurence LEMELLE[24],
Hugues LEROUX[25], Ariel LEONARD[16], Robert LETTIERI[2], William MARCHANT[2],
Larry R. NITTLER[26], Ryan OGLIORE[27], Wei Ja ONG[16], Frank POSTBERG[19], Mark C. PRICE[12],
Scott A. SANDFORD[28], Juan-Angel Sans TRESSERAS[13], Sylvia SCHMITZ[9], Tom SCHOONJANS[29],
Geert SILVERSMIT[29], Alexandre S. SIMIONOVICI[30], Vicente A. SOLÉ[13], Ralf SRAMA[31],
Thomas STEPHAN[15], Veerle J. STERKEN[18,32], Julien STODOLNA[2], Rhonda M. STROUD[6],
Steven SUTTON[23], Mario TRIELOFF[19], Peter TSOU[33], Akira TSUCHIYAMA[34],
Tolek TYLISZCZAK[7], Bart VEKEMANS[29], Laszlo VINCZE[29], Joshua Von KORFF[2],
Naomi WORDSWORTH[35], Daniel ZEVIN[2], and >30,000 Stardust@home dusters[36]

[1]ESCG, NASA Johnson Space Center, Houston, Texas, USA
[2]Space Sciences Laboratory, U.C. Berkeley, Berkeley, California, USA
[3]ARES, NASA Johnson Space Center, Houston, Texas, USA
[4]Robert A. Pritzker Center for Meteoritics and Polar Studies, Field Museum of Natural History, Chicago, Illinois, USA
[5]DESY, Hamburg, Germany
[6]Materials Science and Technology Division, Naval Research Laboratory, Washington, District of Columbia, USA
[7]Advanced Light Source, Lawrence Berkeley Laboratory, Berkeley, California, USA
[8]IAS Orsay, Orsay, France
[9]Geoscience Institute, Goethe University Frankfurt, Frankfurt, Germany
[10]Space Research Centre, University of Leicester, Leicester, UK
[11]Department of Astronomy, University of Washington, Seattle, Washington, USA
[12]University of Kent, Kent, UK
[13]European Synchrotron Radiation Facility, Grenoble, France
[14]George Washington University, Washington, District of Columbia, USA
[15]University of Chicago, Chicago, Illinois, USA
[16]Washington University, St. Louis, Missouri, USA
[17]SUNY Plattsburgh, Plattsburgh, New York, USA
[18]Max-Planck-Institut für Kernphysik, Heidelberg, Germany
[19]Institut für Geowissenschaften, Universität Heidelberg, Heidelberg, Germany
[20]Max-Planck-Institut für Chemie, Mainz, Germany
[21]Ontario, Canada
[22]Natural History Museum, London, UK
[23]Advanced Photon Source, Argonne National Laboratory, Chicago, Illinois, USA
[24]Ecole Normale Superieure de Lyon, Lyon, France
[25]University Lille 1, Lille, France
[26]Carnegie Institution of Washington, Washington, District of Columbia, USA
[27]University of Hawai'i at Manoa, Honolulu, Hawai'i, USA
[28]NASA Ames Research Center, Moffett Field, California, USA
[29]University of Ghent, Ghent, Belgium
[30]Institut des Sciences de la Terre, Observatoire des Sciences de l'Univers de Grenoble, Grenoble, France

[31]IRS, University Stuttgart, Stuttgart, Germany
[32]IGEP, TU Braunschweig, Braunschweig, Germany
[33]Jet Propulsion Laboratory, Pasadena, California, USA
[34]Osaka University, Osaka, Japan
[35]South Buckinghamshire, UK
[36]Worldwide
[*]Corresponding author. E-mail: david.r.frank@nasa.gov

Abstract–We discuss the inherent difficulties that arise during "ground truth" characterization of the Stardust interstellar dust collector. The challenge of identifying contemporary interstellar dust impact tracks in aerogel is described within the context of background spacecraft secondaries and possible interplanetary dust particles and β-meteoroids. In addition, the extraction of microscopic dust embedded in aerogel is technically challenging. Specifically, we provide a detailed description of the sample preparation techniques developed to address the unique goals and restrictions of the Interstellar Preliminary Exam. These sample preparation requirements and the scarcity of candidate interstellar impact tracks exacerbate the difficulties. We also illustrate the role of initial optical imaging with critically important examples, and summarize the overall processing of the collection to date.

INTRODUCTION

The collection of contemporary interstellar dust particles (ISPs) was a secondary goal of the Stardust mission (Brownlee et al. 2003), but the preliminary examination entailed an intensive 6 yr effort. Prior to capture, Landgraf et al. (1999a) estimated that approximately 120 ISPs (including ~40 > 1 μm) would impact the aerogel in the Stardust interstellar dust collector (SIDC). The extreme scarcity and anticipated sizes of ISPs make their aerogel tracks tremendously elusive. Therefore, since the return of the Stardust samples in 2006, there has been a mammoth effort to identify potential interstellar candidate tracks in the SIDC. Success was made possible only by the Stardust@home project (Westphal et al. 2014a), a unique scientific endeavor that distributed high resolution imaging of the SIDC worldwide to >30,000 volunteers for searching.

In addition to ISP candidates, the identified tracks include secondaries from the spacecraft, and possibly, sporadic interplanetary dust particles (IDPs). We calculated the most likely track angles arising from secondary impacts on the spacecraft, in order to hypothesize a likely origin (primary versus secondary) for a given track without extraction or analysis. We also carried out quantitative dynamical modeling of β-meteoroids and IDPs in bound orbits that emit the zodiacal light. These models can be used to predict the most likely particle trajectories for IDPs at Stardust.

Throughout the paper, we address the inherent scientific and flight-related complexities that prevent non-destructive, unambiguous verification of an interstellar origin for cosmic particle impact tracks. We have also addressed unprecedented sample preparation requirements that do not simply add an additional complication; they compound the challenge in a synergistic way. Consequently, in order to characterize and preserve this unique collection, the Stardust Interstellar Preliminary Examination (ISPE) required a massive collaboration consisting of six independent projects defined by Westphal et al. (2014b): candidate identification via Stardust@home, extraction and photo-documentation, X-ray microprobe characterization, foil crater search and electron beam analysis, dynamical modeling of ISP propagation and known IDP streams, and laboratory simulations of hypervelocity dust impacts in aerogel. Interstellar candidate track extraction and photo-documentation is the second independent project, described here with its relationship to other projects during the ISPE (these other projects are described in detail in the companion papers of this volume). On the basis of what we have learned, we also consider future curatorial options for the collection.

For a total of 195 days in 2000 and 2002, the SIDC was exposed to the interstellar dust flux. Based on measurements by the Galileo and Ulysses satellites (Frisch et al. 1999), a nominal flow direction of 259° ecliptic longitude and 8° ecliptic latitude ($\lambda = 259°$,

α = 8°) was assumed for the Stardust mission. By rotating the spacecraft in the ecliptic and rotating the collector with respect to the spacecraft, the SIDC was oriented so that it remained roughly orthogonal to this assumed flow, throughout both ISP collection periods. This three-axis stabilization was achieved with Stardust's hydrazine propulsion system, but Stardust was permitted to drift by ±15° about each of three perpendicular axes (Hirst and Yen 1999). This three-axis drift is commonly referred to as the spacecraft's "deadband."

The SIDC consisted of two passive collecting media: 0.1039 m^2 of silica aerogel and approximately 1.4 × 10^{-2} m^2 of Al foil. 132 aerogel tiles were inserted into an Al frame and flown under compression that induced moderate fracture. The tile perimeters have undergone varying degrees of cracking and flaking from the tile insertion, removal, and possibly shock stress from the landing. We estimate that approximately 20% of the total space-exposed area is damaged to a degree that prevents optical identification of small (<~100 μm in length) particle impact tracks. Cometary tiles were not as severely damaged, probably because of their higher densities and heights. This made them more robust for tile extraction from the collector tray. To prevent further damage, we took a conservative approach for cutting the Al foils. Our double-blade rotary cutter yielded approximately 77% of space-exposed foil as flat strips. The remaining amount was left attached to the unexposed (folded) portion of the foil and not flattened for scanning electron microscopy. Foil crater searches and analyses during the ISPE are described by Stroud et al. (2014). Optically recognizable particulate contamination is common across most of the aerogel and foil surfaces, and as inclusions within the aerogel. Zolensky et al. (2008) describe witness materials, spacecraft recovery, contamination control, and sample storage facilities at the Johnson Space Center (JSC).

SOURCES OF IMPACT TRACKS

Impact tracks in the aerogel record a particle's trajectory relative to the SIDC. Here, we constrain these trajectories and/or provide probability distributions for background IDPs, β-meteoroids, and spacecraft secondaries. These can be compared to expectations for ISPs. A track's orientation is defined by its zenith (θ) and azimuth (φ). θ is defined as the angle between a track and the vector normal to the cometary collector. If we project the track onto the surface of the collector, φ is the angle between the projection and a "vertical" line across the surface, and is positive when measured clockwise from the zero position. Fig. 1 illustrates these definitions for an arbitrary track.

Interstellar Dust

Updated modeling efforts of the ISP flux take into account the Lorentz force filtering and exclusion of grains from the inner solar system with a relatively large charge to mass ratio (Sterken et al. 2014). Of the 118 total impacts predicted, only approximately 50 were >0.3 μm in diameter. Laboratory simulations by Postberg et al. (2014) and an analysis of detection efficiency by Westphal et al. (2014a) indicate that this particle size is near the detection threshold. If we then assume that 20% of the collecting area is damaged (as described above), we estimate a total of approximately 40 detectable ISP impacts in the SIDC. The dynamics of the ISP population that penetrates through the inner heliosphere are dominated by a parameter β, which is the ratio of solar radiation pressure to solar gravity (Landgraf et al. 1999b). However, unknown material properties for individual ISPs and poorly constrained initial conditions (at the termination shock) introduce substantial uncertainty in the model: the distribution of β is unknown, the average ISP velocity vector has a 2σ range of approximately 78° in ecliptic longitude (Frisch et al. 1999), and the full time-dependent Lorentz force for individual particles is not readily formulated with model accuracy. This combination prevents precise prediction of the ISP velocity distribution at Stardust. Figs. 1–3 by Westphal et al. (2014b) illustrate the expected trajectories of ISPs relative to Stardust's orbit and the SIDC for a range of β values and initial ecliptic longitudes. In addition, the Stardust spacecraft was subjected to a constant 3-axis deadband of ±15°, the result of which is inherent uncertainty in the actual trajectory of a particle (in ecliptic coordinates) with respect to its track. Because of these reasons, rigorous proof of interstellar origin for a given sample will require measurement of anomalous isotopic signatures. Any identification of a bona fide ISP may serve to tighten constraints on the model parameters, initiating a positive feedback loop between the model and observations of the SIDC. In this scenario, a well collimated population of tracks made by particles with similar material properties (i.e., similar β) could perhaps be inferred as interstellar in origin with isotopic data on one of its members. The "midnight tracks" reported by Westphal et al. (2014b) are one such population. On the other hand, particles that are compositionally exotic and/or consist primarily of known presolar phases in chondrites should be excused from destruction while maintaining ISP status.
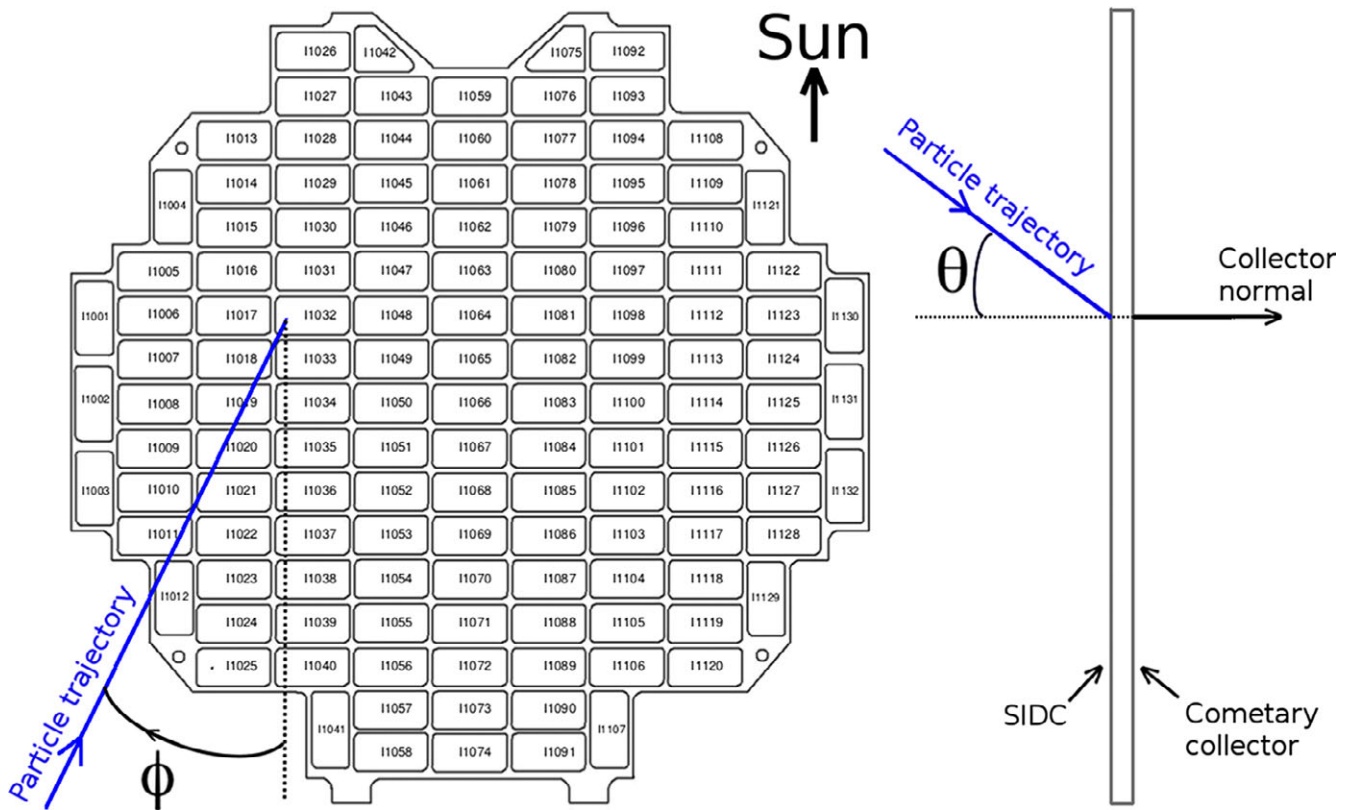
Fig. 1. Schematic of the Stardust Interstellar Dust Collector illustrating the azimuth (ϕ) and zenith (θ) for an arbitrary track. The top view shows the definition of track azimuth, ϕ, with the locations and numbers of the 132 aerogel tiles. The side view illustrates track zenith, θ, measured with respect to the cometary collector normal.

Interplanetary Dust Particles

The IDP "cloud" is continuously fed primarily by cometary emissions and is a potential source of dust in the SIDC. Using observations of the zodiacal light, Nesvorny et al. (2010) derived a distribution of orbital parameters for the majority of the IDPs that make up this cloud. Using these IDP eccentricities and inclinations in a Monte Carlo simulation, we find a strong depletion of the IDP flux within the ecliptic when θ > ~10–20° (Fig. 2a). On the other hand, we find a concentration of the flux at normal incidence (θ < ~10–20°) to the SIDC (Fig. 2b). However, ISP collection occurred within the main asteroid belt at 2.1–2.6 AU, and random asteroid collisions near the time of flight may have contributed to the local dust environment. Such events could conceivably eject micron-sized IDPs within the ecliptic, and with a resulting velocity vector that is rotated (in ecliptic latitude) only approximately 8° from ISPs. With the deadband uncertainty of ±15°, we cannot rule out an unknown number of inadvertently captured "sporadic"

IDPs with trajectories and compositions similar to those predicted for ISPs. However, a subset of these may be decipherable with chemical and mineralogical characterization alone. The observed depletion of S in cold, dense molecular clouds may be present as circumstellar FeS (Keller et al. 2002), and stellar outflows may contribute this phase to the ISM. However, the state of S in the ISM is uncertain, principally because the astronomical observations are limited, probably biased, and are difficult to normalize (Jenkins 2009). But in general, S is not one of the major condensable elements that have observed order-of-magnitude depletion in the diffuse ISM (Draine 2009). On the other hand, sulfides are ubiquitous in all chondritic IDPs, with pentlandite and high-Ni pyrrhotite prevalent among hydrous IDPs as products of aqueous alteration (Zolensky and Thomas 1995; Dai and Bradley 2001). In a practical sense, if a grain in the SIDC is dominated by Fe/Ni sulfides, an interplanetary origin should be suspected. If pentlandite, high-Ni pyrrhotite, and/or phyllosilicates are present, an interplanetary origin may be confirmed.
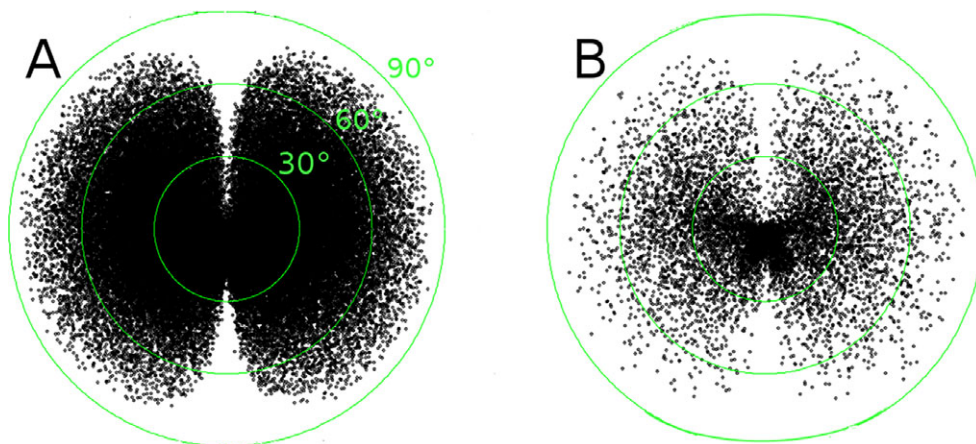
Fig. 2. Monte Carlo simulations of interplanetary dust particle trajectories relative to the Stardust Interstellar Dust Collector, taking into account the longitudinal tracking of the nominal interstellar dust particle flow direction (λ = 259°). Each data point represents a track with θ = its radial coordinate and ϕ = its azimuth. Particle trajectories with ϕ = 0 are above the center and with ϕ = 180 are below the center. Each concentric circle represents 30° in θ. a) The simulation run with 10^5 events shows strong depletion of the flux around the midnight (ϕ = 0) and 6 o'clock (ϕ = 180) directions. b) The same simulation run with 10^4 points shows that concentration occurs near normal incidence.

β-Meteoroids

β-Meteoroids are IDPs that escape from the inner solar system in unbound orbits when solar radiation pressure exceeds solar gravity due to sublimation or fragmentation from collisions (Wehry et al. 2004). One of the science planning constraints in the Stardust Mission Plan (Hirst and Ryan 2002) forbids exposure of the SIDC to the β-meteoroid flux, assumed to be nearly radial in direction. Nevertheless, some exposure was permitted for communication, trajectory correction maneuvers (TCMs), spacecraft deadbanding, and in support of the flyby to asteroid 5535 Annefrank. Here, we demonstrate that these activities were brief in duration and resulted in minimal exposure of the SIDC, but at the expense of exposing the cometary collector.

We assume a radial direction for the β-meteoroid flux. Then, the position vector, $\vec{r}$, of the spacecraft in ecliptic coordinates is continuously parallel to the flux. If we then define a unit vector, $\hat{n}$, normal to the cometary collector, the value of the dot product $\hat{n} \cdot \hat{r}$ gives the effective area of the collector surface exposed to the flux, expressed as a fraction of the total area. This convention outputs positive values during exposure of the SIDC and negative values during exposure of the cometary collector. The values of $\hat{n}$ and $\hat{r}$, at hourly intervals, are obtained from the dataset provided by Farnham and Semenov (2006). These data consist of actual spacecraft orientation computed on board and telemetered to the Deep Space Network. Fig. 3 shows the orientations of $\hat{n}$ and $\hat{r}$ at different times and Fig. 4 contains the

computed values of $\hat{n} \cdot \hat{r}$ throughout the two ISP collection periods. Since an impact in the SIDC is a distinct possibility, while a statistically significant population is likely to have been captured in the cometary aerogel, it is important to understand the allowed trajectories (displayed as track angles). A particular β-meteoroid trajectory (relative to the SIDC) is a function of its speed in the ecliptic, the relative velocity of Stardust, and the orientation of the SIDC at the time of impact. Using data obtained by the Ulysses spacecraft, Wehry et al. (2004) constrains so-called "classical" β-meteoroids in the ecliptic to a range of 20–50 km s^{-1}, although the statistical distribution of speeds is poorly constrained. Nevertheless, we can still constrain the allowed trajectories in the SIDC since there are only a few brief periods when capture is possible. After adopting the collector reference frame, we can calculate the relative arrival speeds and trajectories of β-meteoroids impacting the collectors as a function of time and average speed (in the ecliptic). Fig. 5 plots the allowed values of track zenith (θ) for the minimum and maximum speeds for β-meteoroids in the ecliptic (20 and 50 km s^{-1}), constraining the possibilities for a given time.

During the first collection, the zenith angles for the entire range of β-meteoroid speeds plunge below (and return above) the 90° "cut-off" simultaneously. Estimating the total time-integrated β-meteoroid fluence over those time intervals is straightforward. During the second collection period, there are times when only β-meteoroids with certain speeds will reach the SIDC. To be conservative, we assume the "worst-case" scenario, and accept the entire distribution of
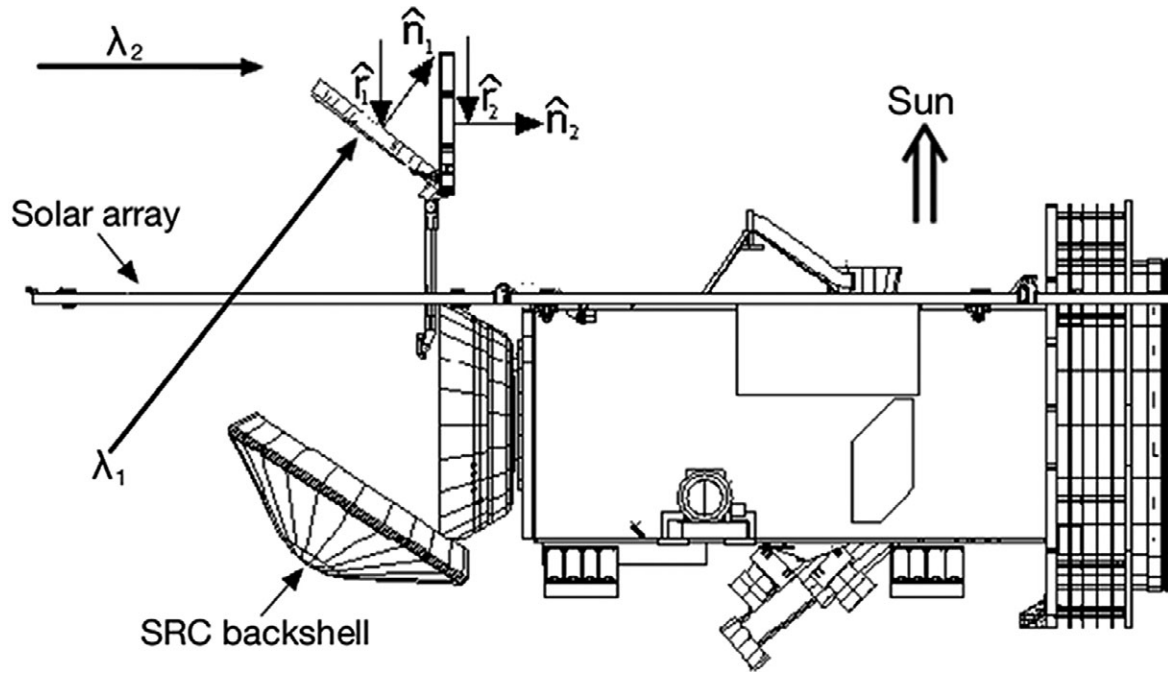
Fig. 3. Collector geometry at different orbital positions (1 and 2). The collector was rotated to different orientations with respect to the spacecraft such that the assumed trajectory ($\lambda = 259°$ longitude in ecliptic) of the interstellar dust stream was orthogonal to the Stardust Interstellar Dust Collector. That is, $\lambda_1 = \lambda_2 = 259°$. At the first position, $\hat{n}_1 . \hat{r}_1 < 0$, and the cometary collector is exposed to the β-meteoroid flux. At the second idealized position, $\hat{n}_2 . \hat{r}_2 = 0$, and neither collector is exposed. Note that these values are independent of a spacecraft rotation about the $\hat{r}$ axes.
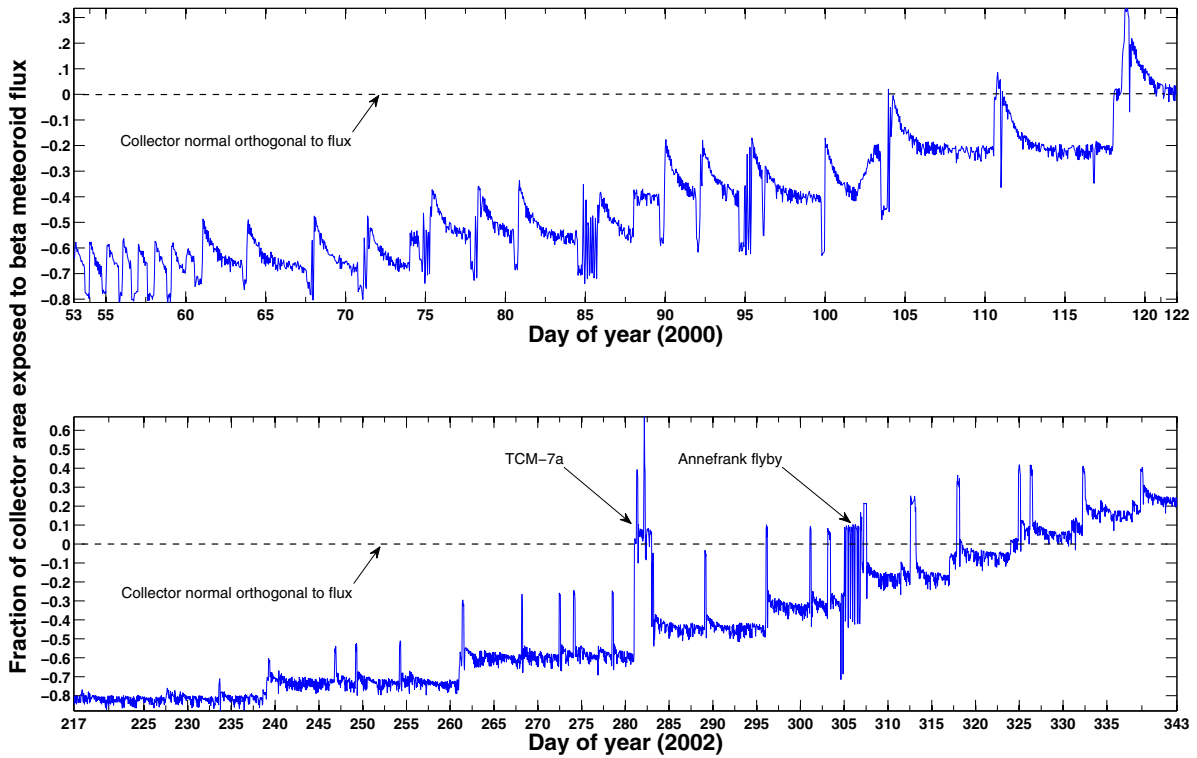

Fig. 4. Collector exposure to the β-meteoroid flux (negative values indicate exposure of the cometary collector). The collection periods during the first and second orbits are shown at top and bottom, respectively. The many sharp peaks denote spacecraft maneuvers for communication and the background "noise" delineates spacecraft deadbanding.
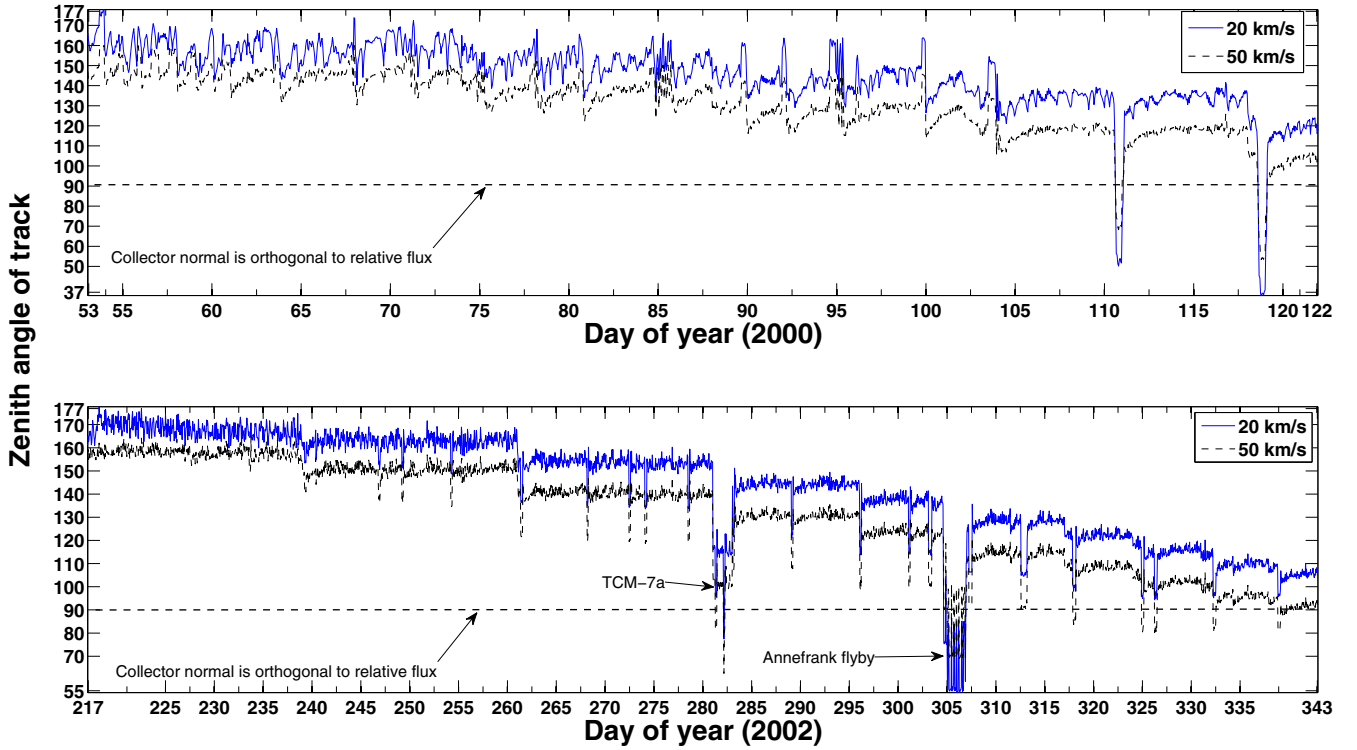
Fig. 5. Allowed zenith (θ) values of β-meteoroid tracks during the two interstellar dust collection periods. θ < 90° indicates a possible time of impact on the Stardust Interstellar Dust Collector. θ = 180° is normal to the cometary collector.

speeds anytime $\theta < 90°$ for any speed. The resulting value is then taken to be an upper limit for the SIDC's fluence estimate.

$$\text{SIDC fluence} < \Delta t \int\limits_{\theta < 90°} \hat{n}(t) \cdot \hat{r}(t) \Psi(t) \, dt \qquad (1)$$

$$\text{Cometary fluence} = -\Delta t \int\limits_{\theta > 90°} \hat{n}(t) \cdot \hat{r}(t) \Psi(t) \, dt \qquad (2)$$

where Ψ is the flux (m^{-2} s^{-1}) and $\Delta t = 3{,}600$ s is the time interval between each value of t. We use the flux measured by the Ulysses spacecraft during its passage through the ecliptic (Wehry et al. 2004). This value at approximately 1.3 AU is 1.5×10^{-4} m^{-2} s^{-1} ± 20%. Since Stardust's ISP collection periods took place at $r = 2.1$–2.6 AU, we can account for the decay of Ψ with a simple r^{-2} dependence.

$$\Psi(1.3 \text{ AU}) = 1.5 \times 10^{-4} \text{ m}^{-2}\text{s}^{-1} \Rightarrow \Psi(r)$$
$$\approx (r/1.3)^{-2}\Psi(1.3) = (2.5 \times 10^{-4} \text{ m}^{-2}\text{s}^{-1})r^{-2} \qquad (3)$$

Finally, letting $\psi = 2.5 \times 10^{-4}$ m^{-2} s^{-1} and $A =$ the area of some region of interest gives the expected number of impacts on the collectors, where N_I

and N_C are the expected number of impacts on the SIDC and cometary collector, respectively. [This article was corrected on 19 July 2013. In the previous sentence and in Equations 4–5, Greek symbols were changed to lowercase psi. Author affiliations were also corrected.]

$$N_I < \psi A \Delta t \int\limits_{\theta < 90°} \hat{n}(t) \cdot \hat{r}(t) [r(t)]^{-2} dt \qquad (4)$$

$$N_C = -\psi A \Delta t \int\limits_{\theta > 90°} \hat{n}(t) \cdot \hat{r}(t) [r(t)]^{-2} dt \qquad (5)$$

Table 1 lists the calculated values of Equations 4 and 5 for the aerogel and aluminum foils on both collectors. We have also put constraints on the arrival speeds and zenith angles. We estimate <0.9 β-meteoroid impacts in the SIDC aerogel and 33 in the cometary aerogel. Track morphology from grains impacting the aerogel at the very high-expected speeds of approximately 26–60 km s^{-1} with nearly radial trajectories should be unique. The model calculations by Wehry et al. (2004) gave a maximum deviation of approximately 20° from the radial direction for the trajectory of a β-meteoroid. If we then take into account

Table 1. Estimated number of β-meteoroid impacts, relative speeds, and zenith angles on the four Stardust collecting media. The lack of a probability distribution for the expected capture speeds and zeniths is due to the uncertain distribution of β-meteoroid speeds. However, given a single value for a β-meteoroid speed (in the ecliptic frame) there is a minor dispersion of approximately 5 km s^{-1} (in the collector frame).

	A (m^2)	First ISP collection	Second ISP collection	Total expected	Relative speeds (km s^{-1})	Allowed zenith[a] (°)
IS aerogel	0.1039	0.065	<0.83	<0.90	28–60	37–90
IS foils	0.01689	0.011	0.13	<0.14	28–60	—
Cometary aerogel	0.1039	14.2	18.9	33.1	26–60	2–90
Cometary foils	0.01689	2.3	3.1	5.4	26–60	—

[a]Measured from each collector normal.
ISP, interstellar dust particle.

a deadband uncertainty of ±15°, we expect to only find β-meteoroids with $\phi = 180° \pm \sim35°$. The Sterken et al. (2014) ISP propogation model predicts that ISPs in this region will impact the SIDC at <~10 km s^{-1}. The greatest probability of capture in the cometary collector occurred at the beginning of the second ISP collection, with expected impact speeds approximately 30–35 km s^{-1} and zenith approximately $155° < \theta < 178°$. Although some particles from comet 81P/Wild 2 impacted in this range of zenith values, their capture speed was approximately 6.1 km s^{-1}. Tracks made by the β-meteoroids should be uniquely bulbous or crater-like.

Secondaries

During both collection periods, the full solar array was fully exposed to the radial β-meteoroid flux and IDPs with eccentric orbits. Secondaries from the solar panels have been positively identified in both the aerogel and foils. Simulations by Burchell et al. (2012) demonstrated that secondary solar panel material should reach the SIDC, and a solar panel origin is generally confirmed by the presence of Ce, definitive spacecraft material in the glass covers. In some cases, a definitive solar panel origin can be determined by track trajectory. But in most cases, the variable orientation of the collector with respect to the spacecraft (Fig. 3) results in ambiguity with a cosmic origin. Fig. 6 shows the statistical distribution of expected azimuth angles (ϕ) for solar panel secondaries. The midnight direction ($-\hat{r}_2$ in Fig. 3) defines the $\phi = 0$ azimuth.

Because of the sample return capsule (SRC) orientation and line of sight to the collector, secondaries arising from the SRC must result from a nearly anti-sunward projectile. Therefore, β-meteoroids are the most likely projectiles to eject SRC secondaries into the collector. Such a secondary would produce a midnight track, which coincidentally, is a trajectory that is also consistent with an origin in the interstellar dust stream. Again, the ambiguity arises from the variable orientation of the SIDC with respect to the spacecraft.
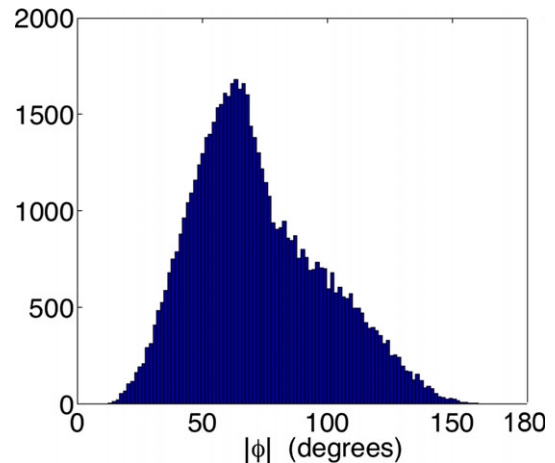

Fig. 6. Statistical distribution of expected azimuth angles for solar panel secondary tracks. The distribution is symmetrical for $\pm\phi$.

For this reason, a detailed understanding of such events is required.

Through a combination of impact experiments with sub-μm enstatite at approximately 16 km s^{-1} into Al targets and subsequent hydrocode modeling, Price et al. (2012) has determined approximate values for the resulting crater diameter, D_C, as a function of projectile diameter, D_p, and projectile speed (up to 30 km s^{-1}). On average, D_C is approximately $5D_p$ in this regime, which closely simulates a β-meteoroid impact. By conservatively assuming that approximately 25% of the crater volume is retained to the surface in the form of an overturned lip due to plastic flow, we estimate that approximately 50 times the volume of the projectile is ejected from the crater. It is therefore highly unlikely for a secondary to be devoid of the target SRC material.

With this in mind, we made a special effort to characterize the material inside the SRC. The standard 6061 Al alloy used for the largest exposed area inside the SRC is known to contain minor amounts of Mg, Si, Ti, Mn, Cr, Fe, Cu, and Zn. In addition, the anodizing likely introduced other contaminants as well. We therefore harvested several small chips from the

Fig. 7. Sampling of the sample return capsule backshell at the Smithsonian Air and Space Museum, showing the locations of 3 of the 5 chips.

SRC, now on display at the Smithsonian Air and Space Museum (Fig. 7). The nature of contaminants with minor abundances was investigated at U.C. Berkeley with a Tescan Vega3 SEM with Oxford X-Max 80 EDX detector, without cleaning. Element maps of the anodized surfaces were conducted at both 5 and 30 keV. Elements detected with >1 atom% were C, O, F, Mg, and S. However, the Mg was found to occur as discrete particles that covered $<5 \times 10^{-4}$ of the surface area and rarely exceeded 1 atom% in these particles. H6107,1 (Fig. 8) consists of material with the largest exposed area in the SRC. Of particular concern was the nature of discrete C/Al inclusions, requiring STXM and transmission electron microscopy (TEM) for characterization. H6107,1 was Pt-coated before an approximately 10 μm wide, 3 μm deep, and 100 nm thick cross section was removed with a FEI Strata 235 Dualbeam Focused Ion Beam (FIB) (Fig. 9). In general, the anodized Al can be identified with X-ray absorption near edge structure (Al-XANES) analysis (Butterworth et al. 2014) in aerogel. However, since the SRC is primarily constructed from Al metal, identification of SRC secondaries in the Al foils may be non-trivial.

ISPE REQUIREMENTS AND TECHNICAL IMPLICATIONS FOR SAMPLE PREPARATION

The unique goals and restrictions of the ISPE are described by Westphal et al. (2014b). The primary motivation for minimizing the thickness of aerogel around the track was to maximize the amount of information that could be gained using scanning transmission X-ray microscopy (STXM). Foremost, the ISPE requirements forbade destructive analyses. Since we did not have a reliable technique for completely

extracting grains < ~5 μm in diameter from aerogel, electron beam analyses were also precluded. With these constraints, STXM became the only available method to quantify the abundances of Mg, Al, and Si. This is critical for ISP candidate characterization. With <30 nm resolution, X-ray absorption imaging and element mapping provide this characterization for terminal particles (TPs), ejected fragments, and track wall residue. When coordinated, STXM XANES and synchrotron X-ray diffraction (SXRD) provide nearly complete characterization of the sub-μm structure of both the amorphous and crystalline components of track wall and terminal grains embedded in aerogel. In addition, synchrotron X-ray fluorescence (SXRF) was required to quantify S and heavier elements, with lower detection limits than STXM. SXRF and SXRD analyses benefit when aerogel background is reduced, but the low energy of a STXM beam requires the surrounding aerogel to be as thin as possible. Finally, sample handling between analyses was an unnecessary risk that was mitigated with a universal configuration. Picokeystones secured between two silicon nitride (Si_3N_4) windows met the stated requirements. In this section we describe the associated sample preparation techniques in detail and address the complications. Details of SXRF, SXRD, and STXM analyses performed during the ISPE are given by Flynn et al. (2014), Brenker et al. (2014), Simionovici et al. (2014), Gainsforth et al. (2014), and Butterworth et al. (2014), respectively.

Mining for Dust in Aerogel: Keystones and Picokeystones

Immediately upon return of the Stardust mission's two aerogel collectors to Earth, whole tracks in the aerogel collector exposed to comet 81P/Wild2 were harvested in wedges of aerogel (typical thickness approximately 500 μm) called "keystones." This is a technically challenging process originally developed by Westphal et al. (2004), which utilizes Sutter MP-285 micromanipulators with <1 μm precision in three axes. To exercise this method, we manufacture borosilicate glass needles to be used as "milling" tools. A Sutter P-2000 micropipette puller can be programmed to consistently pull 1 mm rods to <<1 μm tips. These needles are heated and bent to appropriate angles, and then securely mounted in pin vices that were press-fitted into hollow, stainless steel rods. The rods can be secured to the micromanipulators, fastened to a computer-controlled stage under a compound microscope. We input critical parameters that determine the keystone size and geometry into MATLAB code that compiles an ordered list of micromanipulator motions (matrix of coordinates). Scripts communicate
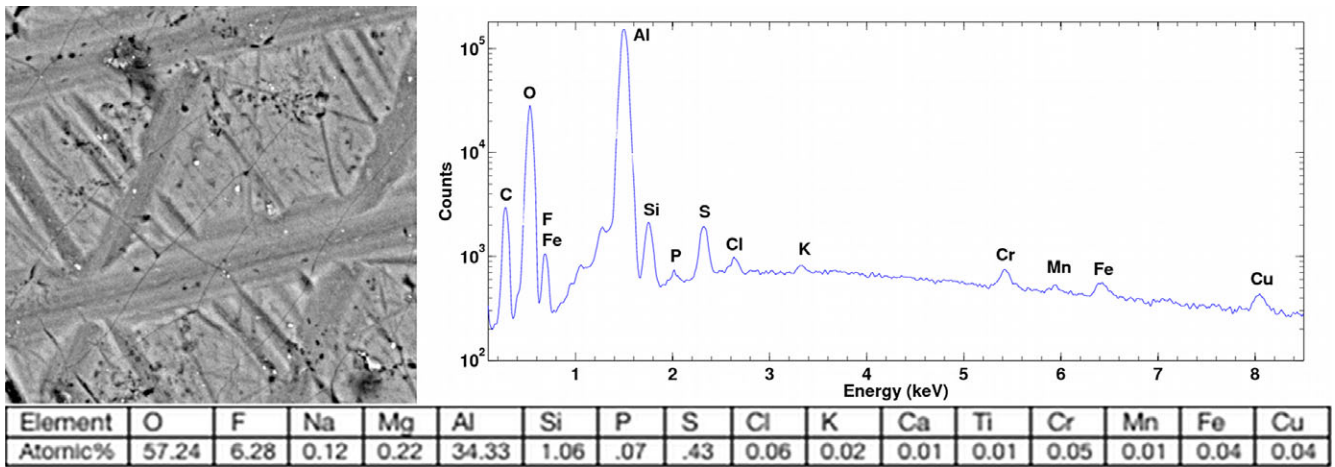
Element	O	F	Na	Mg	Al	Si	P	S	Cl	K	Ca	Ti	Cr	Mn	Fe	Cu
Atomic%	57.24	6.28	0.12	0.22	34.33	1.06	.07	.43	0.06	0.02	0.01	0.01	0.05	0.01	0.04	0.04

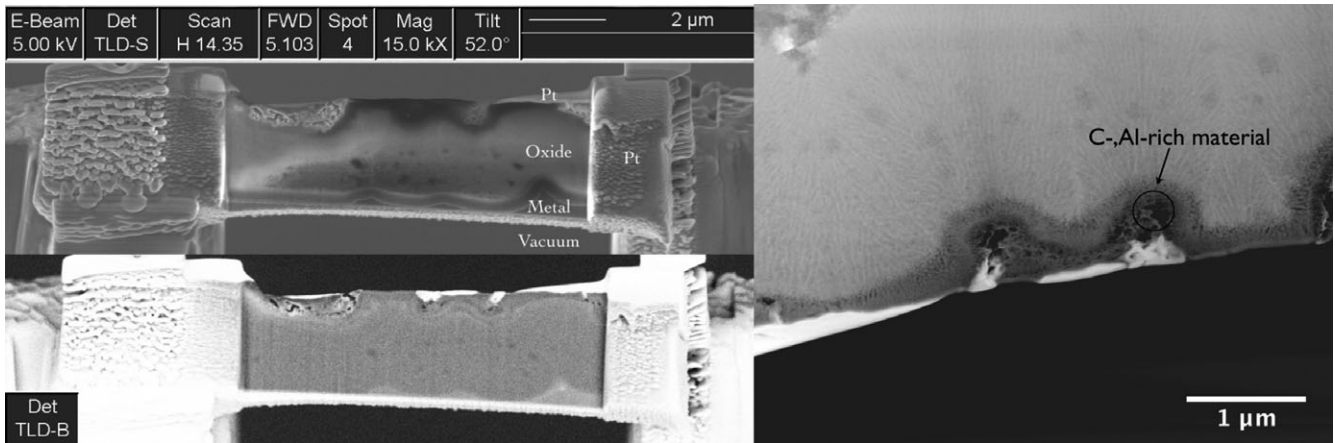Fig. 8. Secondary electron image of H6107,1, with a 200 μm × 200 μm field of view and its EDX spectrum/quantification.

Fig. 9. Focused Ion Beam section from H6107,1. Backscatter and secondary electron images (left) and the "pits" containing an Al/C-rich material (right).

these coordinates to the micromanipulators in order to mill aerogel in an automated fashion. Other details of this automated keystone extraction system for standard cometary keystones have been previously well developed and described; we do not elaborate on them here. Instead, we are concerned here with the challenges unique to extracting candidate interstellar dust impact tracks for analysis and the resulting refinements and new procedures that have been developed.

Westphal et al. (2004) also proposed the concept of a very thin picokeystone for extractions from the SIDC. Picokeystones are similar to their keystone predecessors, but with the aerogel surrounding the track milled out to approximately 70 μm thick (Fig. 10). We named this portion of the picokeystone the "pico," and refer to its thickness as the "pico thickness." This is roughly one-tenth of the thickness of an average cometary keystone. Achieving this level of precision, reliably, required a new set of techniques that were developed on flight

spare aerogel. A great deal of trial and error (i.e., mangling of picokeystones) led to substantial refinements and a routine extraction procedure.

High Precision Aerogel Milling for Picokeystones

Making the critical cuts to carve out the thin slices of aerogel around candidate interstellar dust tracks is a technical challenge. Cutting the aerogel surrounding tracks to a thickness of 70 μm in turn requires needles to pierce the aerogel at a distance of approximately 35 μm on each side of the track. With this tolerance, several corrections to the previously established method were necessary.

During the milling procedure, external vibrations were minimized with a floating vibration isolation table. This was sufficient for cometary keystones where the cutting path was usually placed no less than 100 μm from any track material. However, at the picokeystone
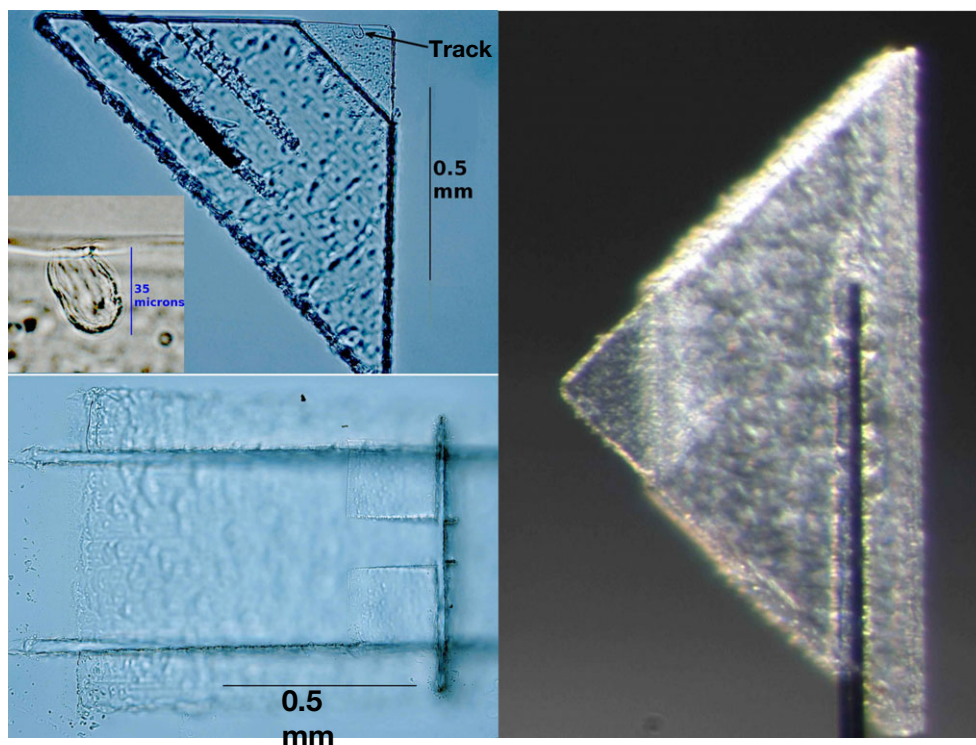
Fig. 10. An illustration of picokeystone geometry. The picokeystones are shown attached to the silicon "microforks" used for extraction from their parent aerogel tiles. At the upper-left is a compound microscope image of the picokeystone I1003,1,40,0,0 that harbors "Sorok," a likely impact by an interstellar grain. The 35 μm deep track is enlarged next to this side view. At the bottom-left, this picokeystone's "quarry," the excavated volume in its parent aerogel tile, is imaged from above. Note the aerogel cut away from the track area still preserved and attached to the quarry. To the right is a blank picokeystone imaged with a stereomicroscope to emphasize its three-dimensional structure. The high precision cuts milled out a smooth sliver of aerogel down to approximately 50 μm thick.

scale, the acceleration of our milling tool by the micromanipulator motors caused vibrations that mangled the surrounding aerogel. By reducing speed and acceleration, we reduced aerogel mangling, but dramatically increased the overall milling duration. A further refinement was necessary, so we maximized the precision and smoothness of the critical milling operations around candidate ISP tracks by achieving the best possible alignment. Previously, we used goniometers to align the needle axes within 1° of the milling axes; acceptable for the cruder, more distant operations from the track material. Our new procedure included this, plus a precise measurement of the needles' alignment error, using the coordinate read-out from the manipulator controller itself. Prior to each extraction, we entered this information into the MATLAB code that compiles the matrix of coordinates into a set of scripts that define the motion of the needles. The needles' motions are then exactly along their axes. To complete a total alignment, we lower the needle to the surface of the aerogel in extremely fine increments until we just slightly "scratch" the surface within approximately 2 μm. When we combined the new

alignment procedure with moderate speeds, we were able to eliminate mangling of the aerogel and achieve unprecedented precision required to mill out picokeystones reliably, and in less than a 48 h period.

An additional pitfall resulted from small (approximately 3 °C) temperature changes in the room. With this amount of change, thermal expansion of the steel rods was significant enough to distort the milling path by an unacceptable amount. Normally, temperatures in the curatorial laboratories at the Johnson Space Center (JSC) are tightly controlled. However, occasional problems with the air-handling unit that supplies conditioned air to the lab can occur without warning. The only viable solution to this problem was to monitor the "critical" cuts that mill out the pico in real time, and allow the other "non-critical" cuts that cut out the main keystone body to be executed overnight.

Preservation of Possible Diffuse Volatiles and Organics

Another concern arose from the picokeystone's fundamental design. The silica aerogel flown on the

Stardust mission has a tremendously high porosity. If an ISP has an organic or volatile component, it may be possible (and in fact quite likely) for it to vaporize and diffuse into the surrounding aerogel upon impact. Evidence of this was observed by Bajt et al. (2009) around impact tracks from comet 81P/Wild 2 particles. For an ISP, the radius of influence from the impact point is highly uncertain. We implemented a new milling sequence that preserves this surrounding aerogel and leaves it attached to the aerogel tile after the picokeystone is extracted, as shown in Fig. 10.

Preservation of Track Trajectory: Tile Removal and "Witness Tracks"

One ISPE requirement was to ensure that track trajectory could be reconstructed, post-extraction, if necessary. These trajectories can be used to identify probable secondaries arising from the spacecraft's solar panels and definitive tracks with a cosmic origin. In general, the surfaces of the aerogel tiles are not exactly parallel to the aluminum collector frame and/or have some topography. Initially, our approach was to conduct the automated scanning for Stardust@home with the entire collector mounted on the scanning system, and to make in situ extractions with this configuration as well. In this scenario, the imagery taken for Stardust@home accurately archives the trajectory of any discovered track. As an additional measure, after precisely aligning and measuring the angle of the 45° needle, we would place one single "witness track" in the region of aerogel to be extracted. By knowing the exact angle and depth of this witness track within a picokeystone, relative to the plane of the collector, reconstructing the impact angle of a track post-extraction is trivial.

The first extractions were carried out in this manner in the Cosmic Dust Lab at JSC. However, an unprecedented and unforeseeable event forced re-evaluation of the extraction procedure. The air handling systems and accompanying networks of electrical control panels on-site at JSC are quite complex. On an otherwise ordinary day, a fluke disconnect in one of the control panels set off a chain reaction of events that ultimately stopped the flow of chilled water to the air-handling unit that supplies air to the Cosmic Dust Lab, while leaving the outside air dampers open. This occurred in August in Houston, TX, so extremely hot and humid outside air was supplied unconditioned to the Cosmic Dust Lab where the temperature is normally maintained around 19 °C. Severe condensation rapidly formed on all of the lab's cold surfaces. Fortunately, this triggered a water alarm in the Cosmic Dust Lab that was installed after a water spill incident in 1985,

and we were able to immediately address the problem. Although the Stardust samples were all sealed in N_2-purged cabinets and not in jeopardy, if the collector had been exposed at the time, damage to the aerogel due to water absorption could have been significant. A high-humidity sensor and alarm system was installed to automatically stop the flow of outside air and ensure the flow of chilled water during a future, unanticipated high-humidity event. Nevertheless, if such an event were to occur overnight, the lab's humidity could remain high enough and linger long enough to dampen its cooler constituents. The curators at JSC considered the risk of exposing the entire collection to a potentially detrimental amount of damage unacceptable. Our initial response was to simply cease cutting operations at the end of each working day and put the collector away in its sealed N_2-purged cabinet. However, this procedure's overwhelmingly impractical, inefficient, and immensely difficult nature quickly became apparent. Consequently, we began to pull individual aerogel tiles from the collector for scanning and extractions, as had been done for cometary tiles. In this scenario, preservation of track trajectory required preservation of tile orientation; a non-trivial demand.

If aerogel behaved like a rigid body, preserving the orientation of the tiles, as they lie in the collector, would be trivial. Changes in the orientation of a tile would then be limited to its three rotational degrees of freedom. However, aerogel is elastic. We know that different manufactured batches of the flown aerogel have different densities and that different aerogel tiles were placed into the collector under varying amounts of compression. The amount of expansion and how uniform it would be after removal from the collector was unknown. In addition, cracks, flaking, and imperfections in the aerogel could result in localized changes during the tile-pulling procedure. To address this issue, we placed an array of 15 witness "tracks" in each aerogel tile prior to removal, recording their precise locations, angles, and depths. In addition, we do the same for the four adjacent aerogel tiles, since cutting the foils exposed on the collecting surface can alter the orientation of those as well.

After the removal of an aerogel tile from the collector, it was mounted in an aluminum clamp for scanning (Fig. 11). We designed these holders to include two major features. First, springs allowed the clamp to be precisely tightened, holding the aerogel so that it was secure enough for making picokeystones, but without causing damage from over-tightening. Second, the holder sat on three vertical screws threaded through the clamp, allowing optimal orientation of the tile surface for scanning and picokeystone extractions. Three silicon chips were attached to the holder with minute droplets
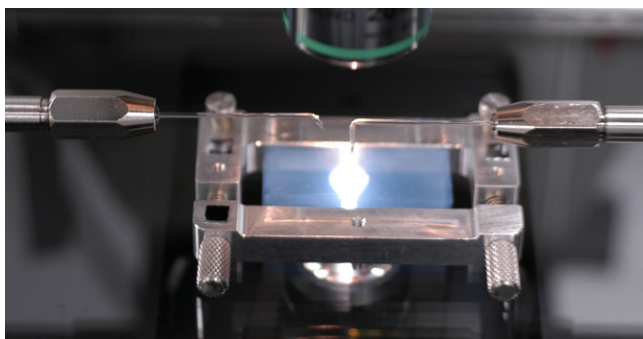
Fig. 11. An aerogel tile mounted in a custom-designed aluminum clamp that facilitates its handling for both automated scanning and extractions. In this image, our needles are being prepared to begin cutting a picokeystone. A $20\times$ objective with a 3.0 cm working distance provides ample space for needle manipulation and ideal magnification for monitoring critical cuts.

of cyanoacrylate to serve as fiducial marks for scanning. We placed the holders on the scanning platform to roughly simulate the orientation at which they sat in the collector and made precise measurements of the fiducial marks' relative positions. After scanning and track identification, we were able to reconstruct the exact track trajectory relative to the plane of the collector, if necessary. By measuring the change in relative witness track positions, we could invert any arbitrary rotation of the aerogel tile as a whole. A close examination of the nearest witness tracks to the real track enabled us to assess the possibility of local distortion. As of this writing, major changes in aerogel structure after tile removal from the collector have not been observed, and this has not been necessary. However, future tiles removed from the SIDC may exhibit such a distortion. Thus, our continued approach is to make every reasonable effort to preserve all of the original particle trajectory information that was imprinted upon the collector.

Picokeystone Mounting for Analysis: Silicon Nitride Windows

Picokeystones require an alternative mount to the standard silicon "microforks" used for cometary keystones that normally hold a keystone very securely with its barbed architecture. There have been occasional reports of lost cometary keystones due to microfork malfunction, either from breakage or after spontaneously falling off the fork-mount. With near-zero sample loss as a goal, this risk was unacceptable. As we refined our extraction procedure using non-flight aerogel, we exploited the picokeystone prototypes to investigate the feasibility of various sample mounts. The silicon microforks used as a standard mount for

cometary keystones continue to be the best tool for the actual removal of a picokeystone from its parent aerogel tile. However, after extraction, we removed the picokeystone from its microforks by hand, carefully applying pressure to the main keystone body with a fine, single hair paintbrush. Using static force, we then used the brush to pick up and place the picokeystone in the well of a Norcada silicon nitride (Si_3N_4) window. We used 70 nm or 50 nm thick windows with a 200 μm deep well. A second Si_3N_4 window was secured on top, either with a micromanipulator and cyanoacrylate, or by fastening custom-machined Al plates with screws (0–80 thread count) and alignment pins (Fig. 12). Use of this mounting jig prevented picokeystone distortion at the moment of assembly. We cut our picokeystones to approximately 430 μm thick so that the main picokeystone body was subjected to just enough compression to hold it firmly during analysis and prevent movement. We conduct this process under a stereomicroscope and use a ^{210}Po low emitting α-source to dissipate excess charge that accumulates on the picokeystone surface and surrounding materials that can result in random, chaotic movements. With an average mass of approximately 3.5 μg, picokeystones can acquire a large charge to mass ratio, and have been known to fly away.

This mounting configuration is extremely advantageous. The Si_3N_4 sandwich is fixed to an aluminum mount that was designed to be compatible with the different X-ray microprobe beams used throughout the ISPE, eliminating risky handling and remounting by investigators. These robust, semi-permanent homes were also designed to protect the samples and minimize the possibility of contamination and damage during analysis and transport. Moreover, in the unlikely event that the thin section of aerogel containing the track separates itself from the main keystone body, during shipping or some other violent episode, the track would not be lost.

STXM Requirements and Pico Thickness

The main goal of STXM measurements during the ISPE was the analysis of the major elements C, O, Mg, Al, Si, and Fe. The attenuation of STXM's soft X-rays by silica aerogel is a function of beam energy, aerogel density, and sample thickness. We can cut the picokeystone thickness with an uncertainty of approximately ±5 μm, and there is only approximately 0.2 eV uncertainty in STXM's beam energy. Thus, it is unfortunate to have such a wide range of aerogel densities (approximately 10–50 mg cm^{-3}). Not all elements (especially C and O) can be accurately quantified in the denser aerogel, and in the densest, Fe
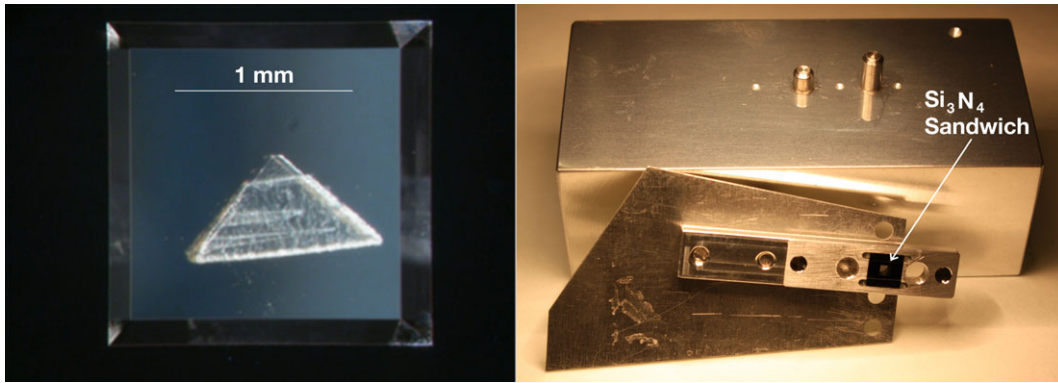
Fig. 12. Si_3N_4 "sandwich" mounting for a picokeystone: On the left, a picokeystone is held securely between two Si_3N_4 windows. On the right, the Si_3N_4 sandwich is fixed in its universal, aluminum mount for analyses. The mounting jig behind this assembly is used to align the Si_3N_4 windows precisely.

is on the edge of detection limits. Initially, we cut our picokeystone prototypes to 50 μm, but making these extractions in situ from the collector was problematic. The foils folded underneath the aerogel tiles partially obscured transmitted light, and the needle cast a dark shadow over our field of view. In addition, we were using a steel rod more than twice as long than for cometary extractions, and this exacerbated the needle vibration. As a precaution, we decided to increase the "standard" pico thickness to 70 μm.

With the technique refined, and applied to single tile extractions post-ISPE, we can be more aggressive in the future with the pico thickness and return to 50 μm standards. It may also be a reasonable risk to even take a 40 μm slice from the denser aerogel, especially if it is required to accommodate X-ray transmission at the 700 eV Fe L-edge. Therefore, knowledge of an aerogel tile's density prior to an extraction is extremely valuable. We can obtain an initial estimate with a measurement of the aerogel's index of refraction (Jurewicz et al. 2007). If there is any significant aerogel density gradient, we should see an extreme value in at least one of the four corners. Or, if practical, a blank picokeystone can be extracted from each tile to have its density measured by STXM. Ultimately, using these density measurements with the following calculations would provide a reliable framework for determining the optimal pico thickness, weighing scientific gain against risk.

The transmission, T, expressed as the ratio of transmitted to incident photon fluence, through a material with density ρ (g cm^{-3}), thickness t (cm), and photoabsorption cross section μ (cm^2 g^{-1}) is readily calculated from

$$T = e^{-\mu\rho t} \quad (6)$$

where μ is a function of beam energy and material. After accounting for attenuation due to both the aerogel

(density ρ_a and thickness t_a) and Si_3N_4 windows (density $\rho_w = 3.44$ g cm^{-3} and thickness t_w), Equation 6 becomes

$$T = e^{-(\mu_a\rho_a t_a + \mu_w\rho_w t_w)} \quad (7)$$

or,

$$t_a = \frac{-\ln T - \mu_w\rho_w t_w}{\mu_a\rho_a} \pm \sim 15\% \quad (8)$$

where μ_a and μ_w are the photoabsorption cross sections for aerogel and Si_3N_4 windows, respectively. The estimated uncertainty arises from the additive uncertainties in μ_w and μ_a. We calculate these values from Lawrence Berkeley National Laboratory's Center for X-ray Optics (CXRO) values at http://henke.lbl.gov/optical_constants/. Generally, these are thought to be accurate within ±10% (Butterworth et al. 2012), so we assume a total uncertainty of approximately ±15%. Reliable detection of an element limits the pico thickness to a maximum, t_{max} (cm), permitting at least 5% transmission. But to help ensure at least this amount, we assume the 15% error, and with two 50 nm Si_3N_4 windows, Equation 8 becomes:

$$t_{max} = \frac{0.85(2.996 - 3.440 \times 10^{-5}\mu_w)}{\mu_a\rho_a} \quad (9)$$

It should also be noted that Equation 6 does not apply when the incident beam energy is near the absorption threshold of the target material. In our case, this precludes measurements of N, O, and Si in our samples, but we know that limited Si K-edge measurements are possible against the background SiO_2 aerogel peak at 1847.5 eV, even through the densest aerogel. Therefore, we apply this model to the other
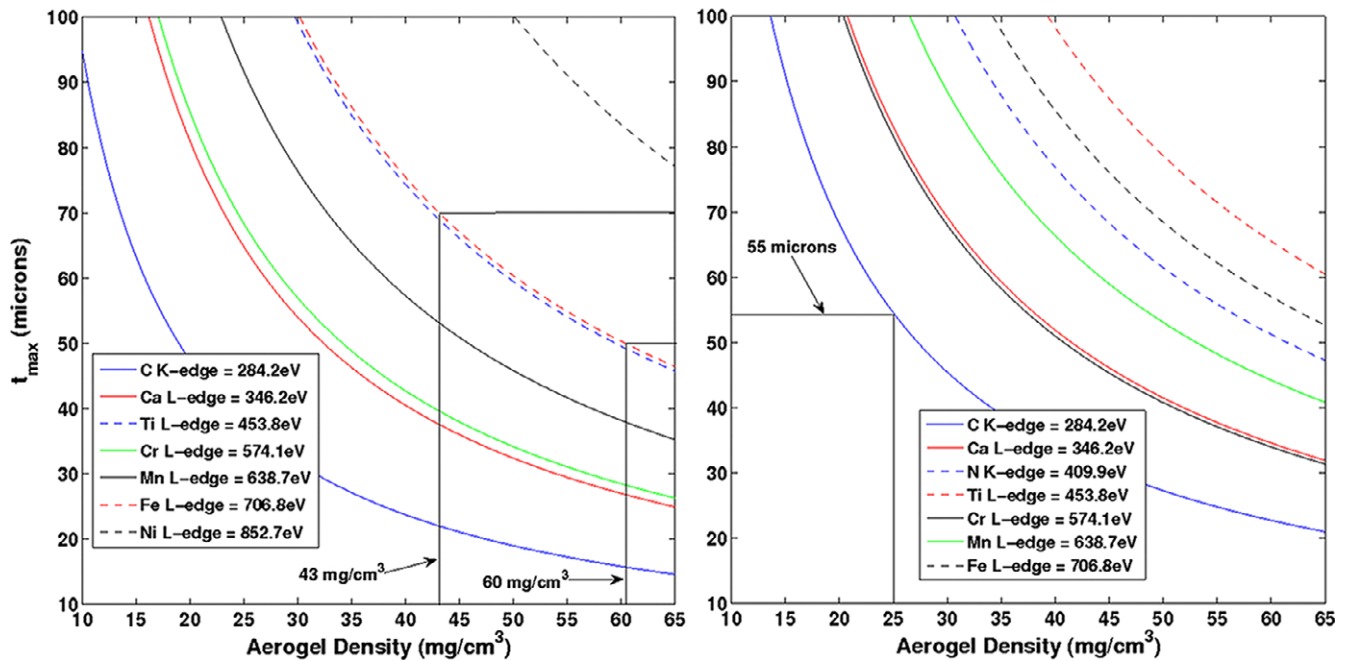
Fig. 13. On the left, the maximum pico thickness, t_{max} (from Equation 9), that permits at least 5% transmission of X-ray photons at the low-energy absorption edges through two 50 nm Si_3N_4 windows and aerogel of varying density. The maximum aerogel densities (43 mg cm^{-3} and 60 mg cm^{-3}) that correspond to at least 5% transmission at the Fe L-edge for 70 and 50 μm picokeystones are shown. On the right, the maximum pico thickness, t_{max} (from Equation 11), that permits at least 5% transmission of X-ray photons at the low-energy absorption edges through aerogel of varying density, mounted *without* Si_3N_4. A 50 μm picokeystone accommodates this for all edge energies through the most common aerogel density (approximately 25 mg cm^{-3}), and for the Fe L-edge energy through even the densest aerogel.

elements that are potentially present in ISPs and IDPs, and the definitive spacecraft contamination Ce. In order of increasing edge energies relevant to STXM analyses, these are Cl, C, Ca, Ti, Cr, Mn, Fe, Ni, Ce, Na, Mg, Al, P, and S. For even the densest aerogel, we find that obtaining adequate transmission through a 70 μm picokeystone in a Si_3N_4 sandwich is ensured for the high edge energies of Ce, Na, Mg, Al, P, and S. For the least dense aerogel, adequate transmission of the 200 eV Cl L-edge is not possible. Therefore, in Fig. 13 we consider the maximum pico thickness, t_{max}, for the remaining elements that may not provide adequate X-ray transmission for detection. That is, elements whose edge energies may not provide adequate transmission for reliable measurements. An additional caution is that minor Mn may not be quantifiable in oxidized phases due to peak overlap with the O K-edge. And in practice, one should consider the largest measured value of ρ, or perhaps a two standard deviation from the mean.

We also consider the option of performing future analyses with the picokeystone still mounted on silicon microforks, rather than being secured between two Si_3N_4 windows. This would eliminate absorption/ attenuation from the Si_3N_4, increasing the range of aerogel densities over which we can detect nitrides and

carbonaceous material. There is also an additional trade-off to consider. The risk of sample degradation or loss during transfer to the Si_3N_4 windows is removed, but loss due to a microfork complication is introduced. Our microforks rest in the cavity of a very thin, hollow glass tube that can easily be shattered if not handled properly. Also, although it is typically obvious during and after extraction if the forks are well attached, we cannot rule out the risk of a picokeystone falling off them. Again, this risk is minimal for a well mounted picokeystone on microforks. A more significant risk to consider is the severance of the pico from the main keystone body. In addition, carbon deposition and other sources of contamination need to be carefully considered. Nevertheless, without Si_3N_4 windows, Equation 6 yields

$$t_a = -\frac{\ln T}{\mu_a \rho_a} \pm \sim 10\% \qquad (10)$$

or

$$t_{max} = \frac{2.696}{\mu_a \rho_a} \qquad (11)$$

where we again have allowed for the estimated uncertainty. These new t_{max} values for the same element
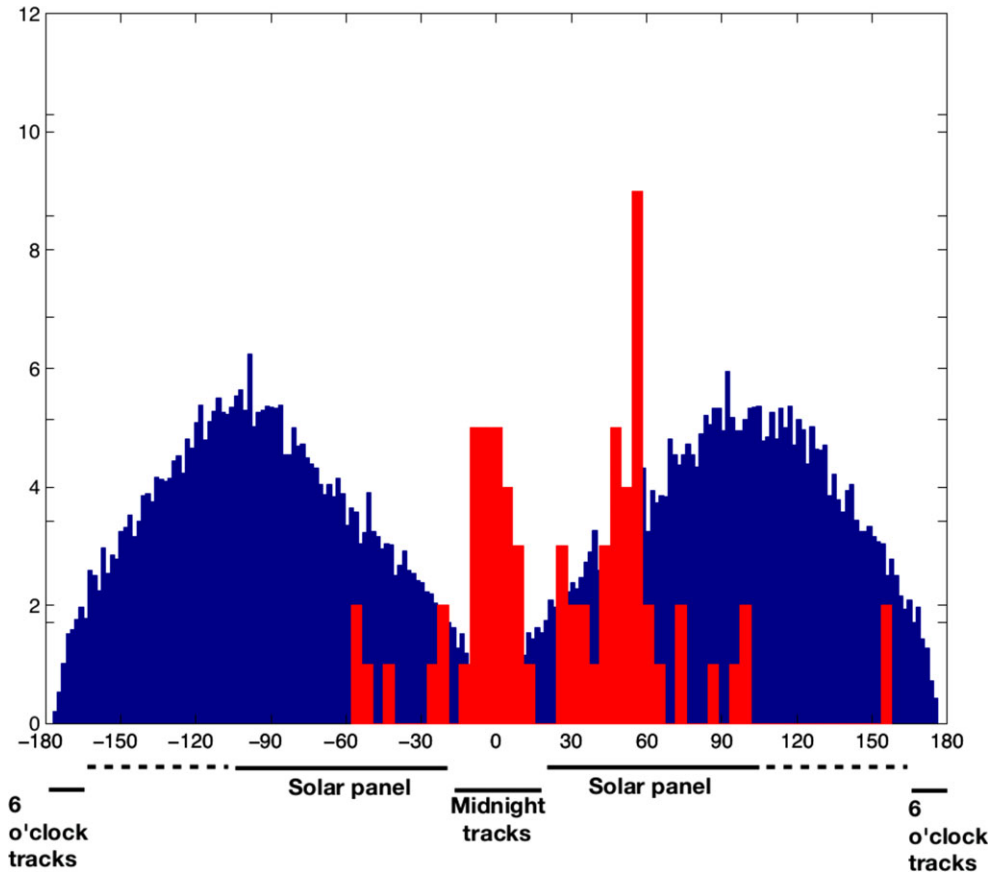
Fig. 14. A histogram of the measured azimuth angles for the 71 unambiguous tracks (red) with the distribution of expected azimuth angles for off-normal interplanetary dust particles (blue) in the background. Also shown is the range of azimuth angles for solar panel secondaries from Fig. 6 (the solid line spans approximately 90% of the distribution and the dashed line contains the remainder). The two tracks at $\phi = 158°$ are nearly parallel and in the same tile, so are very likely to be solar panel secondaries. (see online version for color figure.)

absorption edges as before are shown in Fig. 13. We also now include the absorption edge for N, which may be detectable in samples measured without Si_3N_4 windows. With this configuration, a 50 μm picokeystone of even the densest aerogel would permit at least 5% transmission of X-ray photons at the Fe L-edge. At the most common observed aerogel density of approximately 25 mg cm^{-3}, we see that transmission is adequate for quantification of all elements, including C.

OPTICAL CLASSIFICATION OF TRACKS

After extraction, but prior to mounting between Si_3N_4 windows, we acquired optical images to classify tracks based on morphology and trajectory alone. When compared to simulations, track morphology, track size, and TP size give clues about the impactor's speed and structure. Burchell et al. (2012) demonstrated that tracks arising from impacts off solar panel glass preserve the impact angle within approximately ±0.4°. Therefore,

track trajectory can be used to help distinguish solar panel secondaries, impactors with a possible cosmic origin, and impactors with a definitive cosmic origin. The 71 unambiguous tracks (Westphal et al. 2014a) identified by Stardust@home can be classified into 3 distinct populations, defined by their azimuth ϕ. A histogram of these 71 tracks is displayed in Fig. 14, as a distribution of their azimuth angles in the collector, along with the expected distribution of off-normal ($\theta > \sim20°$) IDP azimuths. Two other populations, discovered by initial optical surveying, have distinct morphologies. In addition, there is a myriad of miscellaneous features that are unlikely due to extraterrestrial particle impacts, but may require extraction and further optical imaging, at a minimum, for confirmation.

6 o'Clock/High Azimuth Tracks

A track displaying a "6 o'clock" azimuth (anti-sunward), such that $|\phi| > 160°$, has no line of sight to
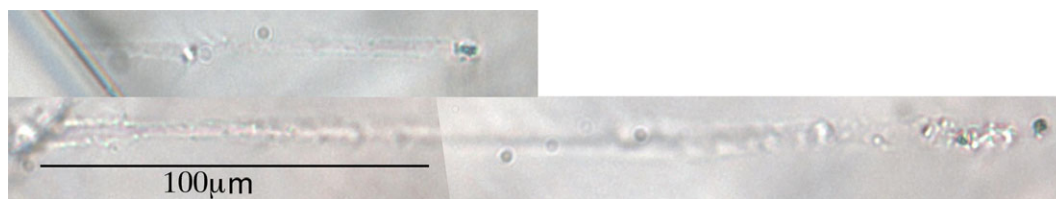
Fig. 15. Secondaries from the solar panel cover glass. I1004,2,3,0,0 (track 3) is displayed above I1017,2,1,0,0 (track 1), the longest track extracted from the Stardust Interstellar Dust Collector.

the spacecraft and is inferred to be of primary cosmic origin. No tracks have been identified in this region. A "high-azimuth" track, such that $20° < |\phi| < 160°$, could either be a solar panel secondary or, possibly, could have a primary cosmic origin. The tracks's zenith and exact location within the collector reduces this range and defines a region (or regions) of certain solar panel secondaries. However, since the collector was rotated (up to 62.6°) from its fully extended position to track the $\lambda = 259°$, $\alpha = 8°$ trajectory, there is inherent ambiguity in the origin of most of these tracks. 46 identified tracks fall in this range of azimuth. Of these, four were extracted during the ISPE and all were confirmed as solar panel secondaries with Ce detection. Consequently, it appears that at least the majority of these tracks have a secondary origin. These include the longest tracks identified and extracted from the SIDC (Fig. 15).

Midnight Tracks

Tracks with $|\phi| < 20°$ (sunward) were named midnight tracks and can either have a cosmic origin or be SRC secondaries. 24 tracks in this region were identified and 13 were extracted. Of these 13, eight were confirmed to be SRC secondaries: seven by the presence of Al metal (Butterworth et al. 2014; Flynn et al. 2014) and one (track 37) by the presence of F (Butterworth et al. 2014). Analyses of track 2 (Table 2) were inconclusive, and this track's TP may require TEM characterization to confirm or rule out the presence of SRC material. Track 38 was too optically dense for STXM analysis, and track 40 contained no detectable residue (see following discussion on bulbous tracks). The remaining two tracks (30 and 34) have compositions that are inconsistent with SRC material (Table 2) and appear to have a cosmic origin. Fig. 16 displays these tracks alongside an SRC secondary, demonstrating their ambiguous morphology. Notice the widening of track 2 near the terminus and the moderately "flattened" appearance of the Orion TP along the direction of impact. In addition, we did not observe any track wall residue. This indicates that these grains may have undergone some degree of plastic deformation but were only subjected to minimal, or no ablation.
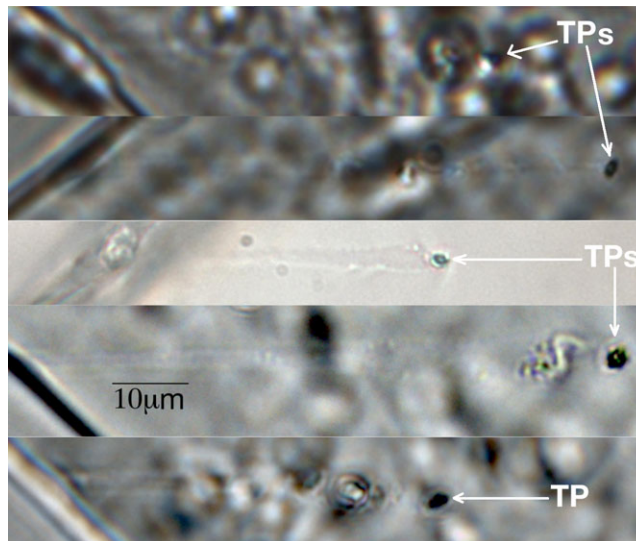

Fig. 16. Optical images of midnight tracks. (Top to bottom) I1047,1,34,0,0 (Hylabrook), I1043,1,30,0,0 (Orion), I1004,1,2,0,0 (track 2), I1092,2,38,0,0 (track 38), and I1097,1,41,0,0 (track 41, a sample return capsule secondary). The initially faint tracks are obscured to an even greater degree by aerogel debris, created during the extraction process, clinging to the picokeystone surface.

Bulbous Tracks

Track 40 (Sorok) (Fig. 17) is a midnight track but had a unique bulbous morphology. It appears to have a likely origin in the interstellar medium, inferred through a combination of optical characterization, simulation comparison, and dynamical modeling. Sorok has a true bulbous morphology, lacking any coarse-grained TPs. Postberg et al. (2014) have shown that impact track morphologies created by sub-μm projectiles (in flight-spare aerogel) underwent important changes at impact speeds approximately 10–15 km s^{-1}. In general, increasing speed increases the track width/length ratio. Since Sorok's residue had a mass below STXM detection limits, it is important to understand the nature of high-speed (>15 km s^{-1}) ejecta hitting the SIDC, in order to determine the likelihood of such an origin. Since Sorok also has a midnight trajectory, we assume a β-meteoroid projectile with the maximum kinetic energy

Table 2. Keystone, picokeystone, and grain extractions performed during the ISPE. As of this writing, tracks 30, 34, and 40 are the ISP candidates.

Tile #	Track	Track type/trajectory	Sample form	Pico (μm)	Track length (μm)	Discernible particles	Analysis references[a]	Analysis summary
I1017	1	Low azimuth	Keystone	N/A	268	(2) 2–3 μm TPs	1,2,3	Mg, Al, K, Ti, Fe, Zn, Ce
I1004	2	Midnight	Keystone	N/A	46	4 × 3 μm TP	2,5	Amorphous Al oxide, S, K, Ti, Cr, Mn, Ni, Cu, Zn
I1004	3	Low azimuth	Keystone	N/A	102	2 μm TP	2,4	Mg, Al, Ce, Zn
I1007	4	Low azimuth	Keystone	N/A	200	1 μm TP	1,3	Na, Mg, Al, Zn, Ce
I1006	5	Low azimuth	Keystone	N/A	114	5 μm TP	1,2,4	Ce, Mg, Al, minor Na
I1029	6	9 o' clock	Picokeystone	70	<5	(5) 2–5 μm TPs	1,2	Corundum, Mg, Na, amorphous Al oxide
I1029	7	9 o' clock	Picokeystone	70	<5	—	—	Lost
I1029	8	9 o' clock	Picokeystone	70	<5	—	—	Lost
I1027	9	Crater	Picokeystone	70	<5	3 μm particle	1,4	Cl, Ti, V, Fe, Cu, Zn
I1029	10	9 o' clock	Picokeystone	70	<5	(3) 1–2 μm TPs	1,2	Weak Na, Al
I1032	11	Crater	Picokeystone	70	<5	—	1,2	Al oxide
I1093	12	Crater	Picokeystone	100	<5	—	1,4	Cr, Cu, Br
I1081	13	Inclusion	Picokeystone	70	<5	—	1,4	Cu, Zn, Se, Br
I1059	14	Crater	Picokeystone	70	<5	—	1,4	Cu, Zn, Se, Br
I1029	15	Crater	Picokeystone	70	<5	—	1,4	Cu, Zn, Se, Br
I1001	16	Crater	Picokeystone	70	<5	—	1,5	Fe, Zn
I1001	17	Crater	Picokeystone	70	<5	—	1,5	Cr, Fe, Ni, Zn
I1006	18	Crater	Picokeystone	70	<5	—	—	Damaged before analysis
I1013	19	Crater	Picokeystone	70	<5	—	1,2	Mg, Al, Si
I1017	20	Crater	Picokeystone	70	<5	—	1,2,3	Cr, Mn, Fe, Ni
I1004	21	Crater	Picokeystone	150	<5	—	1,2,3	Si
I1013	22	Crater	Picokeystone	70	<5	—	—	Damaged before analysis
I1031	23	Crater	Picokeystone	70	<5	—	1,2	Si, minor Na, Al
I1006	24	Crater	Picokeystone	70	<5	—	1,2	Si, minor Al, Fe, Ni, Zn
I1075	25	Crater	Picokeystone	100	<5	—	2,5	K, Ti, V, Cr, Mn, Fe, Cu, Zn
I1093	26	Triangle	Picokeystone	N/A	<5	—	2	None detected
I1093	27	Surface grain	Naked grain	N/A	<5	—	5	Zn
I1060	28	Midnight	Picokeystone	60	66	4 μm TP	2,3	Al metal and Al oxide
I1059	29	Midnight	Picokeystone	100	146	3–4 μm TP	2,3	Al metal
I1043	30	Midnight	Picokeystone	100	75	3–4 μm TP	1,2,3,4,6	Spinel, olivine, amorphous Mg/Si/Al oxide, Fe
I1059	31	"spider"	Picokeystone	120	23	—	2	Mg, metallic/oxidized Al
I1044	32	Crater	Picokeystone	70	10	3 μm sphere	2,5	Si, Ni
I1044	33	Crater	Picokeystone	70	<5	—	2,5	S, K, Ca, Ti, Cr, Mn, Fe, Ni, Cu, Zn
I1047	34	Midnight	Picokeystone	85	57	3–4 μm TP	2,3,6	Mg-rich olivine, Fe, Al

Table 2. *Continued.* Keystone, picokeystone, and grain extractions performed during the ISPE. As of this writing, tracks 30, 34, and 40 are the ISP candidates.

Tile #	Track	Track type/trajectory	Sample form	Pico (μm)	Track length (μm)	Discernible particles	Analysis references[a]	Analysis summary
I1032	35	Midnight	Picokeystone	85	65	4–5 μm TP	2	Al metal & some Al oxide
I1032	36	Midnight	Picokeystone	85	35	—	2	Al metal and amorphous Al oxide
I1092	37	Midnight	Picokeystone	85	62	2–3 μm TP	1,2,3	Amorphous Al oxide, C, minor Fe, F
I1092	38	Midnight	Picokeystone	85	86	3–4 μm TP	2	None; too thick for STXM
I1017	39	Midnight	Picokeystone	85	31	1–2 μm TP	2	Al metal
I1003	40	Midnight/bulbous	Picokeystone	100	34	—	1,2	possible C, Fe
I1097	41	Midnight	Picokeystone	75	50	2 μm TP	2	Al metal
I1048	42	Midnight	Picokeystone	75	37	2 μm TP	2	Al metal

TP: terminal particle.

[a]1: Bechtel et al. (2014); 2: Butterworth et al. (2014); 3: Brenker et al. (2014); 4: Simionovici et al. (2014); 5: Flynn et al. (2014); 6: Gainsforth et al. (2014).

Fig. 17. Bulbous tracks in the Stardust Interstellar Dust Collector. A likely interstellar origin for I1003,1,40,0,0 (Sorok) is inferred from its trajectory and bulbous morphology (left). Lagadha, a larger feature with the same width/length ratio, is imaged from above while still in its parent aerogel tile (right).

derived from the Ulysses measurements by Wehry et al. (2004). By also assuming complete conversion of β-meteoroid kinetic energy into secondary kinetic energy, we find that the maximum kinetic energy of a midnight secondary is $E_{max} = 1.5 \times 10^{-7}$ J. Since we find midnight secondaries in the range of 2–4 μm, we use E_{max} to calculate the maximum speed for a 2 μm Al sphere to be 5.2 km s^{-1}. This is in agreement with their low-speed track morphology. In order to have secondary impacts at >15 km s^{-1}, we require ejecta <0.44 μm in diameter. Fig. 8 by Postberg et al. (2014) is an excellent proxy for this type of impact, showing a 5 μm diameter and 23μm long track produced by a 0.37 μm orthopyroxene projectile at 15 km s^{-1}. Since total track volume increases with projectile kinetic energy (Burchell et al. 2001; Hörz et al. 2009), this figure puts an upper limit on the volume of a high speed (approximately 15 km s^{-1}) secondary. By assuming rotational half-symmetry along the track axis of Sorok, we estimate its volume is approximately $9.3 \times 10^3 \mu m^3$, almost 2 orders of magnitude larger than the estimated maximum volume. We conclude that Sorok cannot be from secondary ejecta.

In addition, we may also have a second track that exhibits an uncanny similarity to Sorok (Fig. 17). "Lagadha" is a feature that has not been extracted and still lies in its parent aerogel tile, I1111,0. Lagadha appears to be a track that impacted the SIDC at nearly normal incidence. If extraction and side profile imaging confirm an unambiguous track, Lagadha will be the largest track identified in the SIDC during the ISPE, and only the second bulbous track. Interestingly, its width/length ratio is identical to that of Sorok, within our low measurement uncertainties of a few microns.

$$\text{Sorok width/length} = (20\mu m \pm 1\mu m)/(33 \pm 1\mu m)$$
$$= 0.606 \pm 8\% = 0.606 \pm 0.048 \quad (12)$$

$$\text{Lagadha width/length} = (90\mu m \pm 5\mu m)/(150\mu m \pm 5\mu m)$$
$$= 0.600 \pm 8.9\% = 0.600 \pm 0.053$$
$$(13)$$

It is unlikely for the only two bulbous tracks in the SIDC to share this ratio so precisely as a matter of coincidence. Therefore, assuming Lagadha is an unambiguous track, we postulate that whatever variables determine this ratio are nearly the same for both Sorok and Lagadha. The survey of tracks in the cometary collector by Burchell et al. (2008) did not reveal any track with a width/length ratio > ~0.5. Postberg et al. (2014) showed that smaller tracks with this type of morphology and track wall texture could be achieved in IS flight spare aerogel with 0.33 μm orthopyroxene at speeds > ~15 km s^{-1}. Presumably, slightly larger tracks with the same ratio could originate from micron-sized particles, with similar composition and crystallinity, at the same speeds. At this speed, Sorok's trajectory is in complete agreement with the expected capture trajectory of an ISP, assuming an astro silicate β-curve (Sterken et al. 2014). However, Kearsley et al. (2012) has confirmed the ratio's dependence on cohesion and sub-grain size at speeds approximately 6 km s^{-1}. Those simulations provide an alternative set of dynamical parameters, demonstrating a possible low-speed, poorly cohesive, or perhaps a purely organic impactor. This would not be at all surprising for an ISP either, given the fractionally large, carbonaceous-bearing component of the interstellar dust flux (Dartois and Muñoz-Caro 2007; Draine 2009).
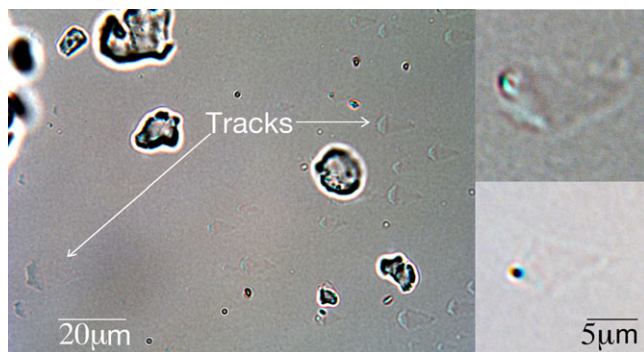
Fig. 18. Tiny tracks in tile I1029,0 known as the "9 o'clock swarm." A field of view with an average track density (left), and two tracks with optically discernible terminal particles (right).

9 o'Clock Swarm

Scattered across an area approximately 8 mm^2 in tile I1029,0 (and possibly others), there was a collection of >10^4 tiny grains that appear to have struck the aerogel at a glancing zenith and $\phi = -90°$. Most of these tracks are 3–20 μm in length and have some variation in morphology themselves, but all have a distinct "ice cream cone" appearance (Fig. 18). Micron-sized TPs are visible at some track terminii, and others appear to harbor disaggregated residue or flattened chips. The survival of an intact particle at the terminus of an approximately 10 μm track implies a relatively low capture speed, but the track width/length ratio of some exceeds 0.7. A low speed, approximately 1 μm crystallite with a poorly cohesive, highly porous, or extremely fine-grained adhering matrix could account for this apparent uniqueness. STXM analyses were performed by Butterworth et al. (2014) on 8 particles extracted in two picokeystones (I1029,1,6 and I1029,4,10). Most of these particles appear to be amorphous fragments with compositions similar to chondrule mesostasis glass, especially that found in some enstatite chondrites (Brearly and Jones 1998). One of the tracks contains a Mg-rich crystalline phase (possibly high-Ca pyroxene) and two 300 nm grains of corundum, indicating a very primitive source with an early formation time, possibly prior to or during CAI formation.

The dense clustering of these tracks with identical trajectories and morphologies indicates that they either originate from local particle disaggregation prior to encounter with the SIDC, or as an ejecta spray from the spacecraft. Although Ce was not detected in any of these 8 particles, we cannot rule out a secondary origin for these particles based solely on composition. Hörz et al. (2000) reported a large swarm of impact tracks in the

Orbital Debris Collector aerogel, and Westphal et al. (2008) discusses the clustering of off-normal impact tracks in the Stardust cometary collector. In both cases, no spacecraft materials have been found and these swarms are attributed to a highly oblique impact on the spacecraft. However, in our case, the apparent trajectory with $\phi = -90°$ and θ very close to 90° had no line of sight to the spacecraft. For this reason, we conclude that a secondary origin for the 9 o'clock swarm is less likely than a local, primary disaggregation.

SUMMARY OF THE ISPE

The tile removal and Stardust@home scanning that took place during the ISPE is shown in Fig. 19 with our current procedure for processing the SIDC summarized in the accompanying flow chart. To date, we have performed automated scanning and Stardust@home searches on approximately 58% of the collector. A total of 47 extractions from the aerogel were made, including 5 blank picokeystones that contained no type of track and were the initial extractions conducted to demonstrate the reliability of our newly established methods on the flown collector. 21 unambiguous tracks, classified into one of the above types, and 21 additional features were extracted for imaging and X-ray microprobe analyses (Table 2). Of the miscellaneous features, 18 picokeystones of shallow, bowl-shaped craters were extracted and found to contain either lodged contaminants or no detectable residue at all, the latter of these attributed to aerogel imperfections and air pockets near the surface. This ruled out unlikely (but nevertheless possible) particle impacts and provided characterization of the particulate contaminants introduced during the manufacturing process (Flynn et al. 2014) and organic contamination accumulated from extraction, packaging, and shipping (Bechtel et al. 2014). Picokeystones of 12 midnight tracks were successfully extracted. Tables 1 and 2 of Stroud et al. (2014) list the 13 foils searched during the ISPE and summarize the 25 crater features analyzed.

DISCUSSION

The number and scope of unknown variables with large uncertainties, the extreme scarcity and elusive nature of collected material, and the unprecedented complications associated with sample preparation compound to make basic characterization of the SIDC far more scientifically and technically challenging than any other collection of extraterrestrial materials. Because of these reasons, a near-term goal to find definitive proof of interstellar dust in the SIDC is unrealistic. A long term, comprehensive plan that
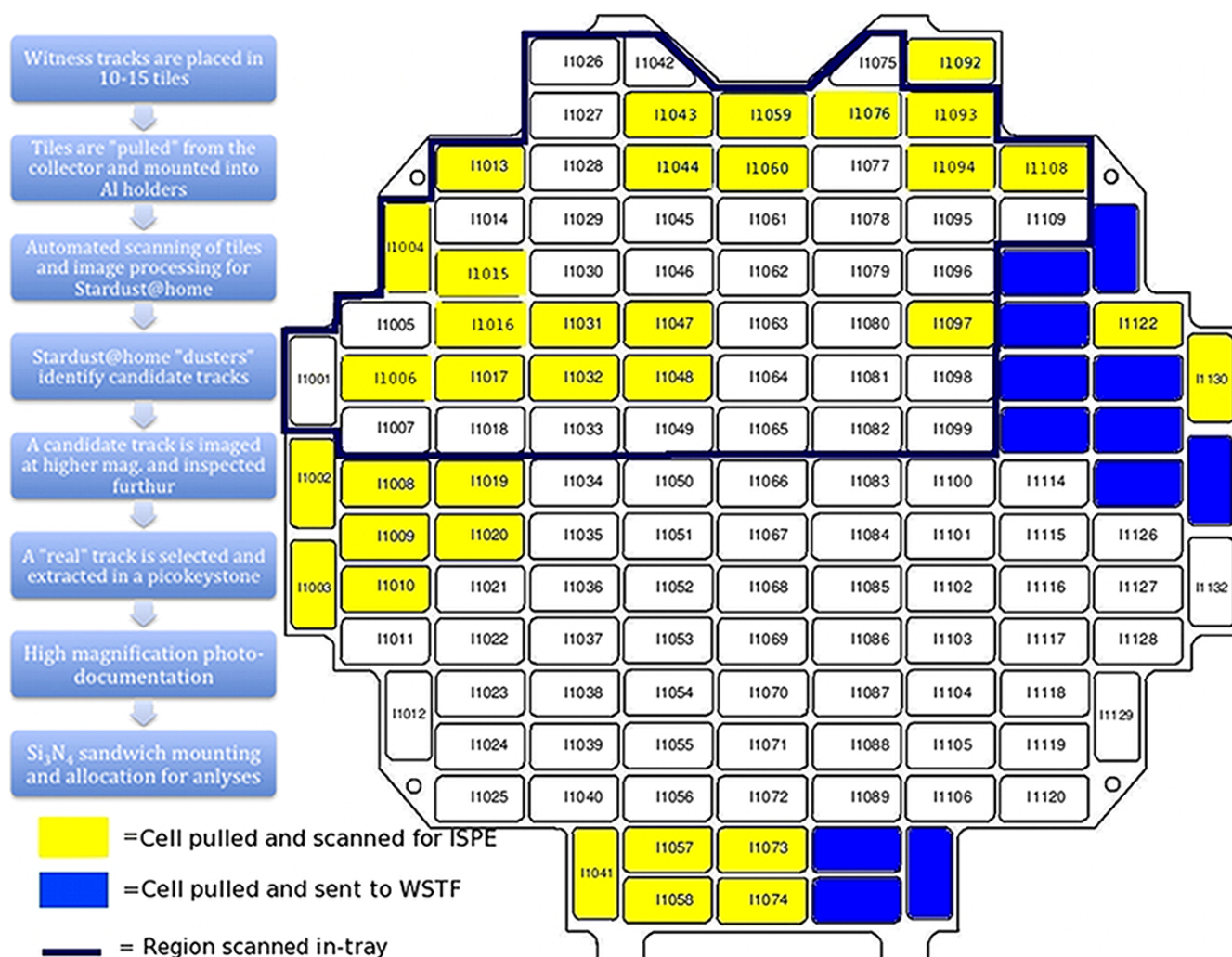
Fig. 19. Overall processing of the Stardust Interstellar Dust Collector at the end of the Stardust Interstellar Preliminary Examination with a flow chart summarizing its chronological processing. WSTF, White Sands Test Facility remote storage.

expands upon the ISPE and ultimately performs isotopic (and necessarily destructive) analyses of interstellar candidates for positive identification certainly is realistic. However, this will require a new generation of sample processing techniques to reliably isolate micron and sub-μm particles. Analysis of scant residue in tracks such as Sorok may still require future technological developments that improve the precision of in situ analysis of dust in aerogel. Our discussion of track morphology demonstrates the need for a comprehensive database of laboratory simulations over a wide range of aerogel densities, impact speeds, and materials. Ultimately, as we learn more, updates to the existing dynamical model will be necessary. Still, the most critical element by far is also the simplest: continued optical scanning and distribution en masse for searching, the only remotely practical means we

currently have to identify the outrageously subtle tracks in a non-destructive way.

We have identified a total of 3 unambiguous, primary cosmic particle impacts in the aerogel and 4 in the foils. The dimensions and morphologies of the foil craters indicate impactors in the approximate size range of 200−450 nm (Stroud et al. 2014). Although we have small statistics, the total foil area searched was <1% of the total aerogel area searched. This amounts to a detected particle density approximately 130 times greater in the foils. Given a set of dynamical parameters for two impacting particles (one in the foil and one in aerogel), the foil crater will have a significantly larger diameter/depth ratio compared to the aerogel track. When this larger ratio is combined with SEM imaging, we obtained detection sensitivity high enough for these sub-μm particles that were undetected in the aerogel.

On the other hand, we have seen that impacts of large (>1 μm) particles in aerogel are efficiently detected and have a greater chance of preserving their primary mineralogy (Gainsforth et al. 2014).

Unexpected results of the ISPE include implications for the cometary collector. Improvements to our aerogel milling technique have been applied to cometary keystones as well, resulting in overall improvement of keystone quality and mounting reliability. We have also shown that β-meteoroid capture was likely and that ISP collection was possible. This will require us to re-examine the cometary aerogel with new eyes and a higher sensitivity for finding small tracks (<~100 μm in length). We became accustomed to treating each collector individually, as separate collections. But in reality, Stardust exposed a single collector with two opposing surfaces to the interplanetary dust environment and returned a cornucopia of extraterrestrial dust: pristine cometary, interplanetary, and contemporary interstellar grains.

Editorial Handling—Dr. John Bradley

REFERENCES

Bajt S., Sandford S. A., Flynn G. J., Matrajt G., Snead C. J., Westphal A. J., and Bradley J. P. 2009. Infrared spectroscopy of Wild 2 particle hypervelocity tracks in Stardust aerogel: Evidence for the presence of volatile organics in cometary dust. *Meteoritics & Planetary Science* 44:471–484.

Bechtel H. A., Flynn G., Allen C., Anderson D., Ansari A., Bajt S., Bastien R. S., Bassim N., Borg J., Brenker F. E., Bridges J., Brownlee D. E., Burchell M., Burghammer M., Butterworth A. L., Changela H., Cloetens P., Davis A. M., Doll R., Floss C., Frank D., Gainsforth Z., Grün E., Heck P. R., Hillier J. K., Hoppe P., Hudson B., Huth J., Hvide B., Kearsley A., King A. J., Lai B., Leitner J., Lemelle L., Leroux H., Leonard A., Lettieri R., Marchant W., Nittler L. R., Ogliore R., Ong W. J., Postberg F., Price M. C., Sandford S. A., Tresseras J. S., Schmitz S., Schoonjans T., Silversmit G., Simionovici A. S., Solé V. A., Srama R., Stephan T., Sterken V. J., Stodolna J., Stroud R. M., Sutton S., Trieloff M., Tsou P., Tsuchiyama A., Tyliszczak T., Vekemans B., Vincze L., Korff J. V., Westphal A. J., Wordsworth N., Zevin D., Zolensky M. E., and >30,000 Stardust@home dusters. 2014. Stardust Interstellar Preliminary Examination III: Infrared spectroscopic analysis of interstellar dust candidates. *Meteoritics & Planetary Science*, doi:10.1111/maps.12125.

Brownlee D. E., Tsou P., Anderson J. D., Hanner M. S., Newburn R. L., Sekanina Z., Clark B. C., Hörz F., Zolensky M. E., Kissel J., McDonnell J. A. M., Sandford S. A., and Tuzzolino A. J. 2003. Stardust: Comet and interstellar dust sample return mission. *Journal of Geophysical Research (Planets)* 108, E10, 8111.

Burchell M. J., Creighton J. A., Cole M. J., Mann J., and Kearsley A. T. 2001. Capture of particles in hypervelocity impacts in aerogel. *Meteoritics & Planetary Science* 36:209–221.

Burchell M. J., Fairey S. A. J., Wozniakiewicz P., Brownlee D. E., Hörz F., Kearsley A. T., See T. H., Tsou P., Westphal A., Green S. F., Trigo-Rodríguez J. M., and Dominguez G. 2008. Characteristics of cometary dust tracks in Stardust aerogel and laboratory calibrations. *Meteoritics & Planetary Science* 43:23–40.

Burchell M. J., Cole M. J., Price M. C., and Kearsley A. T. 2012. Experimental investigation of impacts by solar cell secondary ejecta on silica aerogel and aluminum foil: Implications for the Stardust interstellar dust collector. *Meteoritics & Planetary Science* 47:671–683.

Butterworth A. L., Westphal A. J., Tyliszczak T., Gainsforth Z., Stodolna J., Frank D. R., Allen C., Anderson D., Ansari A., Bajt S., Bastien R. S., Bassim N., Bechtel H. A., Borg J., Brenker F. E., Bridges J., Brownlee D. E., Burchell M., Burghammer M., Changela H., Cloetens P., Davis A. M., Doll R., Floss C., Flynn G., Grün E., Heck P. R., Hillier J. K., Hoppe P., Hudson B., Huth J., Hvide B., Kearsley A., King A. J., Lai B., Leitner J., Lemelle L., Leroux H., Leonard A., Lettieri R., Marchant W., Nittler L. R., Ogliore R., Ong W. J., Postberg F., Price M. C., Sandford S. A., Sans Tresseras J., Schmitz S., Schoonjans T., Silversmit G., Simionovici A. S., Solé V. A., Srama R., Stephan T., Sterken V. J., Stroud R. M., Sutton S., Trieloff M., Tsou P., Tsuchiyama A., Vekemans B., Vincze L., Korff J. V., Wordsworth N., Zevin D., Zolensky M. E., and >30,000 Stardust@home dusters. 2014. Stardust Interstellar Preliminary Examination IV: Scanning transmission X-ray microscopy analyses of impact features in the Stardust interstellar dust collector. *Meteoritics & Planetary Science*, doi:10.1111/maps.12220.

Butterworth A., Becker N., Gainsforth Z., Lanzirotti A., Newville M., Proslier T., Stodolna J., Sutton S., Tyliszczak T., Westphal A. J., Zasadzinski J. 2012. New homogeneous standards by atomic layer deposition for

synchrotron X-ray fluorescence and absorption spectroscopies (abstract #2666). 43rd Lunar and Planetary Science Conference. CD-ROM.

Brearly A. and Jones R. 1998. Chondritic meteorites. *Reviews in Mineralogy* 36:1–398.

Brenker F. E., Schoonjans T., Silversmit G., Vekemans B., Vincze L., Westphal A. J., Allen C., Anderson D., Ansari A., Bajt S., Bastien R. S., Bassim N., Bechtel H. A., Borg J., Bridges J., Brownlee D. E., Burchell M., Burghammer M., Butterworth A. L., Changela H., Cloetens P., Davis A. M., Doll R., Floss C., Flynn G., Fougeray P., Frank D. R., Gainsforth Z., Grün E., Heck P. R., Hillier J. K., Hoppe P., Hudson B., Huth J., Hvide B., Kearsley A., King A. J., Lai B., Leitner J., Lemelle L., Leroux H., Leonard A., Lettieri R., Marchant W., Nittler L. R., Ogliore R., Ong W. J., Postberg F., Price M. C., Sandford S. A., Sans Tresseras J., Schmitz S., Simionovici A. S., Solé V. A., Srama R., Stephan T., Sterken V. J., Stodolna J., Stroud R. M., Sutton S., Trieloff M., Tsou P., Tsuchiyama A., Tyliszczak T., Korff J. V., Wordsworth N., Zevin D., and Zolensky M. E., and >30,000 Stardust@home dusters. 2014. Stardust Interstellar Preliminary Examination V: XRF analyses of interstellar dust candidates at ESRF ID13. *Meteoritics & Planetary Science*, doi:10.1111/maps.12206.

Dai Z. R. and Bradley J. P. 2001. Iron-nickel sulfides in anhydrous interplanetary dust particles. *Geochimica et Cosmochimica Acta* 65:3601–3612.

Dartois E. and Muñoz-Caro G. M. 2007. Carbonaceous dust grains in luminous infrared galaxies. Spitzer/IRS reveals a-C:H as an abundant and ubiquitous ISM component. *Astronomy & Astrophysics* 476:1235–1242.

Draine B. T. 2009. Interstellar dust models and evolutionary implications. *Cosmic Dust-Near and Far, ASP Conference Series* 414:453–472.

Farnham T. L. and Semenov B. 2006. Stardust dust collector geometry. NASA Planetary Data System SDU-C-SRC-6-GEOMETRY-V1.0.

Flynn G., Sutton S., Lai B., Wirick S., Allen C., Anderson D., Ansari A., Bajt S., Bastien R. S., Bassim N., Bechtel H. A., Borg J., Brenker F. E., Bridges J., Brownlee D. E., Burchell M., Burghammer M., Butterworth A. L., Changela H., Cloetens P., Davis A. M., Doll R., Floss C., Frank D. R., Gainsforth Z., Grün E., Heck P. R., Hillier J. K., Hoppe P., Hudson B., Huth J., Hvide B., Kearsley A., King A. J., Leitner J., Lemelle L., Leroux H., Leonard A., Lettieri R., Marchant W., Nittler L. R., Ogliore R., Ong W. J., Postberg F., Price M. C., Sandford S. A., Tresseras J. S., Schmitz S., Schoonjans T., Silversmit G., Simionovici A., Solé V. A., Srama R., Stephan T., Sterken V. J., Stodolna J., Stroud R. M., Trieloff M., Tsou P., Tsuchiyama A., Tyliszczak T., Vekemans B., Vincze L., Korff J. V., Westphal A. J., Wordsworth N., Zevin D., and Zolensky M. E., and >30,000 Stardust@home dusters 2014. Stardust Interstellar Preliminary Examination VII: Synchrotron X-ray fluorescence analysis of six Stardust interstellar candidates using the Advanced Photon Source 2-ID-D microprobe. *Meteoritics & Planetary Science*, doi:10.1111/maps.12144.

Frisch P. C., Dorschner J. M., Geiss J., Greenberg J. M., Grün E., Landgraf M., Hoppe P., Jones A. P., Krätschmer W., Linde T. J., Morfill G. E., Reach W., Slavin J. D., Svestka J., Witt A. N., and Zank G. P. 1999. Dust in the local interstellar wind. *The Astrophysical Journal* 525:492–516.

Gainsforth Z., Brenker F. E., Burghammer M., Simionovici A. S., Schmitz S., Cloetens P., Lemelle L., Sans Tresseras J., Schoonjans T., Silversmit G., Solé V. A., Vekemans B., Vincze L., Westphal A. J., Allen C., Anderson D., Ansari A., Bajt S., Bastien R. S., Bassim N., Bechtel H. A., Borg J., Bridges J., Brownlee D. E., Burchell M., Butterworth A. L., Changela H., Davis A. M., Doll R., Floss C., Flynn G., Frank D. R., Grün E., Heck P. R., Hillier J. K., Hoppe P., Hudson B., Huth J., Hvide B., Kearsley A., King A. J., Lai B., Leitner J., Leroux H., Leonard A., Lettieri R., Marchant W., Nittler L. R., Ogliore R., Ong W. J., Postberg F., Price M. C., Sandford S. A., Srama R., Stephan T., Sterken V. J., Stodolna J., Stroud R. M., Sutton S., Trieloff M., Tsou P., Tsuchiyama A., Tyliszczak T., Korff J. V., Wordsworth N., Zevin D., Zolensky M. E., and >30,000 Stardust@home dusters. 2014. Stardust Interstellar Preliminary Examination VIII: Identification of crystalline material in two interstellar candidates. *Meteoritics & Planetary Science*, doi:10.1111/.maps.12148.

Hirst E. A. and Yen C. W. 1999. Stardust mission plan. Jet Propulsion Laboratory Mission Plans: http://pdssbn.astro.umd.edu/holdings/sdu-a-navcam-2-edr-annefrank-v1.0/document/mission_plan.pdf

Hirst E. A. and Ryan R. E. 2002. Stardust mission plan post launch supplement B, Wild 2 encounter test: Annefrank flyby. Jet Propulsion Laboratory Mission Plans: http://pdssbn.astro.umd.edu/holdings/sdu-a-navcam-2-edr-annefrank-v1.0/document/m_plan_supb.pdf

Hörz F., Zolensky M., Bernhard R., See T., and Warren J. 2000. Impact features and projectile residues in aerogel exposed on Mir. *Icarus* 147:559–579.

Hörz F., Cintala M. J., See T. H., and Nakamura-Messenger K. 2009. Penetration tracks in aerogel produced by Al_2O_3 spheres. *Meteoritics & Planetary Science* 44:1243–1264.

Jenkins E. 2009. A unified representation of depletions in the interstellar medium. *The Astrophysical Journal* 700:1299–1348.

Jurewicz A. J. G., Jones S. M., Zolensky M., Frank D., Dupray L., and deHoog B. 2007. Stardust aerogel baseline data: recovery and use (abstract #1897). 38th Lunar and Planetary Science Conference. CD-ROM.

Kearsley A. T., Burchell M. J., Price M. C., Cole M. J., Wozniakiewicz P. J., Ishii H. A., Bradley J. P., Fries M., and Foster N. J. 2012. Experimental impact features in Stardust aerogel: How track morphology reflects particle structure, composition, and density. *Meteoritics & Planetary Science* 47:737–762.

Keller L. P., Hony S., Bradley J. P., Molster F. J., Waters L. B. F. M., Bouwman J., de Koter A., Brownlee D. E., Flynn G. J., Henning T., and Mutschke H. 2002. Identification of iron sulphide grains in protoplanetary disks. *Nature* 417:148–150.

Landgraf M., Müller M., and Grün E. 1999a. Prediction of the in-situ dust measurements of the Stardust mission to comet 81P/Wild 2. *Planetary and Space Science* 47:1029–1050.

Landgraf M., Augustsson K., Grün E., and Gustafson B. A. S. 1999b. Deflection of the local interstellar dust flow by solar radiation pressure. *Science* 286:2319–2322.

Nesvorný D., Jenniskens P., Levison H. F., Bottke W. F., Vokrouhlický D., and Gounelle M. 2010. Cometary origin of the zodiacal cloud and carbonaceous micrometeorites. Implications for hot debris disks. *The Astrophysical Journal* 713:816–836.

Price M. C., Kearsley A. T., Burchell M. J., Howard L. E., Hillier J. K., Starkey N. A., Wozniakiewicz P. J., and Cole M. J. 2012. Stardust interstellar dust calibration: Hydrocode modeling of impacts on Al-1100 foil at velocities up to 300 km s^{-1} and validation with experimental data. *Meteoritics & Planetary Science* 47:684–695.

Postberg F., Hillier J. K., Armes S. P., Bugiel S., Butterworth A. L., Dupin D., Fielding L. A., Fujii S., Gainsforth Z., Grün E., Li Y. W., Srama R., Sterken V. J., Stodolna J., Trieloff M., Westphal A. J., Allen C., Anderson D., Ansari A., Bajt S., Bastien R. S., Bassim N., Bechtel H. A., Borg J., Brenker F. E., Bridges J., Brownlee D. E., Burchell M., Burghammer M., Changela H., Cloetens P., Davis A. M., Doll R., Floss C., Flynn G., Frank D. R., Heck P. R., Hoppe P., Hudson B., Huth J., Hvide B., Kearsley A., King A. J., Lai B., Leitner J., Lemelle L., Leroux H., Leonard A., Lettieri R., Marchant W., Nittler L. R., Ogliore R., Ong W. J., Price M. C., Sandford S. A., Tresseras J. S., Schmitz S., Schoonjans T., Silversmit G., Simionovici A., Solé V. A., Stephan T., Stroud R. M., Sutton S., Tsou P., Tsuchiyama A., Tyliszczak T., Vekemans B., Vincze L., Korff J. V., Wordsworth N., Zevin D., Zolensky M. E., and >30,000 Stardust@home dusters. 2014. Stardust Interstellar Preliminary Examination IX: High speed interstellar dust analogue capture in Stardust flight-spare aerogel. *Meteoritics & Planetary Science*, doi:10.1111/maps.12173.

Simionovici A. S., Lemelle L., Cloetens P., Solé V. A., Sans Tresseras J., Butterworth A. L., Westphal A. J., Gainsforth Z., Stodolna J., Allen C., Anderson D., Ansari A., Bajt S., Bassim N., Bastien R. S., Bechtel H. A., Borg J., Brenker F. E., Bridges J., Brownlee D. E., Burchell M., Burghammer M., Changela H., Davis A. M., Doll R., Floss C., Flynn G., Frank D. R., Grün E., Heck P. R., Hillier J. K., Hoppe P., Hudson B., Huth J., Hvide B., Kearsley A., King A. J., Lai B., Leitner J., Leonard A., Leroux H., Lettieri R., Marchant W., Nittler L. R., Ogliore R., Ong W. J., Postberg F., Price M. C., Sandford S. A., Schmitz S., Schoonjans T., Schreiber K., Silversmit G., Srama R., Stephan T., Sterken V. J., Stroud R. M., Sutton S., Trieloff M., Tsou P., Tsuchiyama A., Tyliszczak T., Vekemans B., Vincze L., Korff J. V., Wordsworth N., Zevin D., Zolensky M. E., and >30,000 Stardust@home dusters. 2014. Stardust Interstellar Preliminary Examination VI: Quantitative elemental analysis by synchrotron X-ray fluorescence nanoimaging of eight impact features in aerogel. *Meteoritics & Planetary Science*, doi:10.1111/maps.12208.

Sterken V. J., Westphal A. J., Altobelli N., Grün E., Hillier J. K., Postberg F., Srama R., Allen C., Anderson D., Ansari A., Bajt S., Bastien R. S., Bassim N., Bechtel H. A., Borg J., Brenker F. E., Bridges J., Brownlee D. E., Burchell M., Burghammer M., Butterworth A. L., Changela H., Cloetens P., Davis A. M., Doll R., Floss C., Flynn G., Frank D. R., Gainsforth Z., Heck P. R., Hoppe P., Hudson B., Huth J., Hvide B., Kearsley A., King A. J., Lai B., Leitner J., Lemelle L., Leroux H., Leonard A., Lettieri R., Marchant W., Nittler L. R., Ogliore R., Ong W. J., Price M. C., Sandford S. A., Tresseras J. S., Schmitz S., Schoonjans T., Silversmit G., Simionovici A., Solé V. A., Stephan T., Stodolna J., Stroud R. M., Sutton S., Trieloff M., Tsou P., Tsuchiyama A., Tyliszczak T., Vekemans B., Vincze L., Korff J. V., Wordsworth N., Zevin D., Zolensky M. E., and >30,000 Stardust@home dusters. 2014. Stardust Interstellar Preliminary Examination X: Impact speeds and directions of interstellar grains on the Stardust dust collector. *Meteoritics & Planetary Science*, doi:10.1111/maps.12219.

Stroud R. M., Allen C., Anderson D., Ansari A., Bajt S., Bassim N., Bastien R. S., Bechtel H. A., Borg J., Brenker F. E., Bridges J., Brownlee D. E., Burchell M., Burghammer M., Butterworth A. L., Changela H., Cloetens P., Davis A. M., Doll R., Floss C., Flynn G., Frank D. R., Gainsforth Z., Grün E., Heck P. R., Hillier J. K., Hoppe P., Huth J., Hvide B., Kearsley A., King A. J., Lai B., Leitner J., Lemelle L., Leroux H., Leonard A., Lettieri R., Marchant W., Nittler L. R., Ogliore R., Ong W. J., Postberg F., Price M. C., Sandford S. A., Sans Tresseras J., Schmitz S., Schoonjans T., Silversmit G., Simionovici A. S., Solé V. A., Srama R., Stephan T., Sterken V. J., Stodolna J., Sutton S., Trieloff M., Tsou P., Tsuchiyama A., Tyliszczak T., Vekemans B., Vincze L., Korff J. V., Westphal A. J., and Zevin D. 2014. Stardust Interstellar Preliminary Examination XII: Identification and elemental analysis of impact craters on Al foils from the Stardust interstellar dust collector. *Meteoritics & Planetary Science*, doi:10.1111/maps.12136.

Westphal A. J., Bastien R. K., Borg J., Bridges J., Brownlee D. E., Burchell M. J., Cheng A. F., Clark B. C., Djouadi Z., Floss C., Franchi I., Gainsforth Z., Graham G., Green S. F., Heck P. R., Horányi M., Hoppe P., Hörz F. P., Huth J., Kearsley A., Leroux H., Marhas K., Nakamura-Messenger K., Sandford S. A., See T. H., Stadermann F. J., Teslich N. E., Tsitrin S., Warren J. L., Wozniakiewicz P. J., and Zolensky M. E. 2008. Discovery of non-random spatial distribution of impacts in the Stardust cometary collector. *Meteoritics & Planetary Science* 43:415–429.

Westphal A. J., Anderson D., Butterworth A. L., Frank D. R., Hudson B., Lettieri R., Marchant W., Korff J. V., Zevin D., Ardizzone A., Campanile A., Capraro M., Courtney K., Crumpler D., Cwik R., Gray F. J., Imada G., Karr J., Lau Wan Wah L., Mazzucato M., Motta P. G., Spencer R. C., Woodrough S. B., Santoni I. C., Sperry G., Terry J., Wordsworth N., Yanke T., Sr., Allen C., Ansari A., Bajt S., Bastien R. S., Bassim N., Bechtel H. A., Borg J., Brenker F. E., Bridges J., Brownlee D. E., Burchell M., Burghammer M., Changela H., Cloetens P., Davis A. M., Doll R., Floss C., Flynn G., Gainsforth Z., Grün E., Heck P. R., Hillier J. K., Hoppe P., Huth J., Hvide B., Kearsley A., King A. J., Lai B., Leitner J., Lemelle L., Leroux H., Leonard A., Nittler L. R., Ogliore R., Ong W. J., Postberg F., Price M. C., Sandford S. A., Tresseras J. S., Schmitz S., Schoonjans T., Silversmit G., Simionovici A. S., Solé V. A., Srama R., Stephan T., Sterken V. J., Stodolna J., Stroud R. M., Sutton S., Trieloff M., Tsou P., Tsuchiyama A., Tyliszczak T., Vekemans B., Vincze L., Zolensky M. E., and >30,000 Stardust@home dusters. 2014a. Stardust Interstellar Preliminary Examination I: Identification of tracks in aerogel. *Meteoritics & Planetary Science*, doi:10.1111/maps.12168.

Westphal A. J., Bechtel H. A., Brenker F. E., Butterworth A. L., Flynn G., Frank D. R., Gainsforth Z., Hillier J. K., Postberg F., Simionovici A. S., Sterken V. J., Stroud R. M., Allen C., Anderson D., Ansari A., Bajt S., Bastien R. S., Bassim N., Borg J., Bridges J., Brownlee D. E., Burchell M., Burghammer M., Changela H., Cloetens P., Davis A. M., Doll R., Floss C., Grün E., Heck P. R., Hoppe P.,

Hudson B., Huth J., Hvide B., Kearsley A., King A. J., Lai B., Leitner J., Lemelle L., Leroux H., Leonard A., Lettieri R., Marchant W., Nittler L. R., Ogliore R., Ong W. J., Price M. C., Sandford S. A., Sans Tresseras J., Schmitz S., Schoonjans T., Silversmit G., Solé V. A., Srama R., Stephan T., Stodolna J., Sutton S., Trieloff M., Tsou P., Tsuchiyama A., Tyliszczak T., Vekemans B., Vincze L., Korff J. V., Wordsworth N., Zevin D., Zolensky M. E., and >30,000 Stardust@home dusters. 2014b. Final reports of the Stardust Interstellar Preliminary Examination. *Meteoritics & Planetary Science*, doi:10.1111/maps.12221.

Westphal A. J., Snead C., Butterworth A., Graham G. A., Bradley J. P., Bajt S., Grant P. G., Bench G., Brennan S., and Pianetta P. 2004. Aerogel keystones: Extraction of complete hypervelocity impact events from aerogel collectors. *Meteoritics & Planetary Science* 39:1375–1386.

Wehry A., Krüger H., and Grün E. 2004. Analysis of Ulysses data: Radiation pressure effects on dust particles. *Astronomy & Astrophysics* 419:1169–1174.

Zolensky M. E. and Thomas K. L. 1995. Iron and iron-nickel sulfides in chondritic interplanetary dust particles. *Geochimica et Cosmochimica Acta* 59:4707–4712.

Zolensky M., Nakamura-Messenger K., Fletcher L., and See T. 2008. Curation, spacecraft recovery, and preliminary examination of the Stardust mission: A perspective from the curatorial facility. *Meteoritics & Planetary Science* 43:5–21.